Quantum computation in silicon-vacancy centers based on nonadiabatic geometric gates protected by dynamical decoupling

M.-R. Yun,[1] Jin-Lei Wu,[1,*] L.-L. Yan,[1,2] Yu Jia,[1,2,3,†] Shi-Lei Su,[1,2,‡] and C.-X. Shan[1,§]

[1]*School of Physics and Laboratory of Zhongyuan Light, Zhengzhou University, Zhengzhou 450001, China*

[2]*Institute of Quantum Materials and Physics, Henan Academy of Sciences, Zhengzhou 450046, China*

[3]*Key Laboratory for Special Functional Materials of Ministry of Education, and School of Materials and Engineering, Henan University, Kaifeng 475001, China*

Due to a strong zero-phonon-line emission, narrow inhomogeneous broadening, and stable optical transition frequencies, the quantum system consisting of negatively charged silicon-vacancy (Si-V) centers in diamond is highly anticipated for application in the development of universal quantum computation. We propose to implement quantum computation using Si-V centers placed in a one-dimensional phononic waveguide, for which quantum gates are realized in a nonadiabatic geometric way and protected by dynamical decoupling (DD). The scheme has the feature of geometric quantum computation, which is robust for controlling errors, and the advantage of DD, which is insensitive to environmental impact. Furthermore, the encoding of qubits in long-lifetime ground states of silicon-vacancy centers can reduce the effect of spontaneous emission. Numerical simulations demonstrate the practicability of the Si-V-center system for quantum computation and the robustness improvement of quantum gates by DD pulses. This scheme may provide a promising path toward high-fidelity geometric quantum computation in solid-state systems.

I. INTRODUCTION

Diamond color centers have great potential in various applications, such as quantum computation [1–5], state detection [6], coherent manipulation [7], and nanoscale sensing [8]. Among the most widely studied solid defects in diamond, the nitrogen-vacancy (N-V) center [9,10], due to its bright and stable luminescence properties and long electron-spin coherence time, is widely used in quantum computation [2–5], state detection [6], coherent manipulation [7], and nanoscale sensing applications [8,11]. However, the development of N-V centers is limited by the characteristics of weak and unstable optical transitions [12]. Recently, the negatively charged silicon-vacancy (Si-V^-, abbreviated as Si-V) center has attracted great attention. The Si-V center is formed by replacing two adjacent carbon atoms in the diamond lattice with a silicon atom, and the silicon atom is located between two vacancies. Due to its D_{3d} point-group symmetry that can protect it from optical inhomogeneity [13–20], the Si-V center can realize practicable initialization and readout of qubits

[21,22]. The scalability of Si-V centers can be achieved by a one-dimensional (1D) phononic waveguide [23,24] and a photonic crystal cavity [25]. In addition, the narrow width (around 5 nm) [26], zero-phonon-line (ZPL) emission [27], and optical coherence properties of Si-V centers in diamond lay the foundation for quantum computation [28]. So far, the Si-V center has been very much favored in different quantum information processes, including entanglement generation [25,29], spin-squeezed-state preparation [30,31], and topological phase simulation [32]. Based on these studies, achieving quantum computing in Si-V centers is highly anticipated.

Quantum computation based on the geometric phase relies on the global characteristics rather than the specific details of evolution. The geometric phase has inherent noise-resilience features against certain local noises, making it a valuable resource for fault-tolerant quantum computation [33,34]. The development of the geometric phase has progressed from the initial adiabatic Abelian phase (Berry phase) [35] to the adiabatic non-Abelian phase [36], and then to the nonadiabatic Abelian phase [37] and nonadiabatic non-Abelian phase (Aharonov-Anandan phase) [38]. Based on these phases, adiabatic Abelian geometric quantum computation (GQC) [39], adiabatic non-Abelian GQC [40], nonadiabatic Abelian GQC (NGQC) [41, 42], and nonadiabatic non-Abelian GQC [43] have been

*jlwu517@zzu.edu.cn
†jiayu@zzu.edu.cn
‡slsu@zzu.edu.cn
§cxshan@zzu.edu.cn

proposed successively. In recent years, various optimization methods have been considered for combination with NGQC, such as optimal control [44–46], time-optimal techniques [47,48], shortened path methods [49,50], non-cyclic schemes [51,52], a reverse-engineering scheme [53–56], and so on [57–62]. These methods have been demonstrated in different platforms, including superconducting circuits [63,64], trapped ions [65,66], and N-*V* centers in diamond [67,68], showing the robust plasticity of GQC with respect to controlling errors.

Given that a quantum system will inevitably be influenced by its environment, destroying the quantum information therein, various methods have been proposed to prevent quantum systems from destruction by environmental impact, including decoherence-free subspace [69–76], noiseless subsystems [77–80], and dynamical decoupling (DD) [81–85]. Among these methods, DD is attractive due to its low resource consumption and excellent performances [82,86–94]. DD counteracts the interaction between the system and environment by using suitable external instantaneous intense pulse sequences, which can effectively improve the immunity of the quantum system to the external environment. These rapid intense pulse sequences can be regarded as a generalization of spin-echo experiments [95] that approximately eliminate the effect of unwanted interactions. DD combined with logic gates has also been established and developed [87,89,94,96]. As another scheme to improve the noise resistance of quantum systems, the method of dynamical error correction (DEC) [97,98] has also attracted a lot of attention. Different from DD, DEC relaxes the pulse-shape assumption, but it will come at the cost of a more complex search for identifying distinct primitive gate sequences with the same leading error [99]. To further reduce the impact of control errors on the system, more complex composite pulses are needed. With the development of technology, the sampling frequency of an arbitrary waveform generator has rapidly developed, reaching several hundreds of Gsamples per second, which can achieve precise bang-bang control. Here, to facilitate operation and achieve quantum computing that is robust to environmental noise and control errors, combining NGQC with DD can protect quantum gates by averaging out decoherence caused by the interaction between qubits and their environment, making it a valuable tool for quantum computation applications.

Here, we propose to implement quantum computation with DD-protected nonadiabatic geometric gates in a hybrid system consisting of Si-*V* centers placed in a 1D phononic diamond waveguide. The Si-*V* centers are coupled to each other by strong strain, with a fixed distance between adjacent centers. To realize quantum gates, we encode the qubits in the long-lifetime ground states of the Si-*V* centers, which are well-suited for this purpose. To improve the system's immunity to the environment, we apply the DD technique by introducing a sequence of rapid pulses that eliminate the impact of the environment on the system. Our work presents an alternative approach to realizing NGQC in Si-*V* centers, with several advantages. First, Si-*V* centers are stable and easy to operate, and their qubits are insensitive to spontaneous emission. Second, we use the geometric phase to realize quantum computation, which has built-in robustness against certain local noises. Finally, DD pulse sequences almost completely eliminate the impact of the environment on the system, making our scheme immune to decoherence caused by environmental factors.

II. PHYSICAL MODEL AND EFFECTIVE HAMILTONIAN

A color center is a defect of a solid-state material, consisting of lattice vacancies and impurity atoms. Due to the wide band gap of diamond, it is an interesting defect color center. As one of the most prominent color centers in diamond, the N-*V* center has a considerable coherence time, and its properties are preserved at room temperature. However, when the optical detection is limited to the ZPL, only $3 - 5\%$ of the N-*V* emission is found in the ZPL. Compared to the N-*V* center, the spectrum of the Si-*V* center is dominated by a ZPL at 1.68 eV, approximately 80% of the emission is concentrated in the ZPL.

A. Physical model and its Hamiltonian

Si-*V* centers are largely protected by symmetry from the optical inhomogeneity. In this section, we introduce the electronic structure of the Si-*V* center at length. The Si-*V* consists of 11 electrons (six from C dangling bonds; four from Si; and one from a nearby donor site, accounting for the negative charge state), which results in a single unpaired electron in ^2E_g or ^2E_u and ^2A_u, as shown in Fig. 1(a). There is excitation of an electron from the e_u to the e_g level in the ZPL, so only the ground state, ^2E_g, and excited state, ^2E_u, are considered. In this situation, there are both orbital and spin degeneracies. We consider the spin-orbit interaction; the Jahn-Teller (JT) effect (some details in Appendix A) [100], i.e., coupling of the electronic state to vibration modes of the nuclear configuration, which results in a lower symmetry configuration of the electronic system, is unstable; and the Zeeman effect after applying an external magnetic field to lift the degeneracy. If the magnetic field consists of the [111] high-symmetry axis of the Si-*V* center, transitions between states with opposite spin projections are forbidden [101,102]. To allow optical transitions between all levels, the magnetic field with $B = 0.21$ T, and the direction between the magnetic and the [111] high-symmetry axis of the Si-*V* is 70.5° [102], as shown in Fig. 1(b). The resulting Hamiltonian of a single Si-*V* center includes three interaction parts: the spin-orbit coupling, $\hat{H}_{SO}$; the JT interaction, $\hat{H}_{JT}$; and the Zeeman interaction, $\hat{H}_Z$.
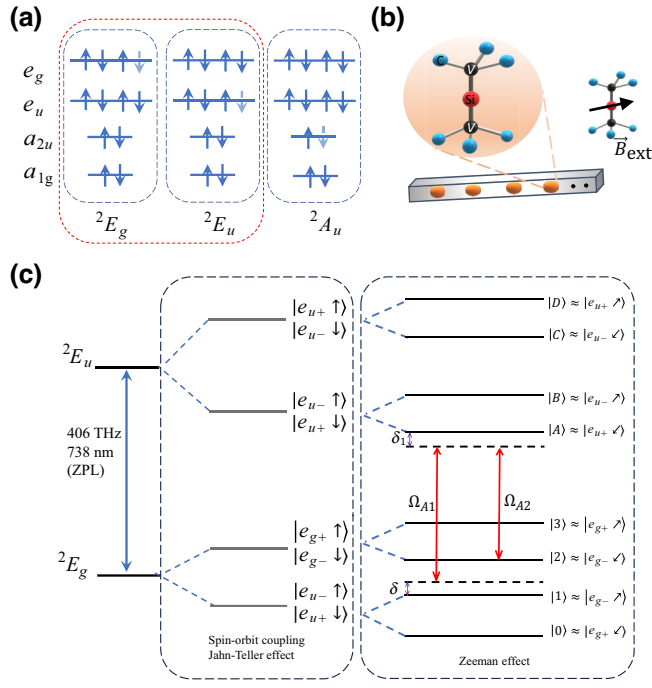
FIG. 1. Si-V electronic structure. (a) Predicted structure of unperturbed Si-V. Blue arrows indicate electrons, and dashed arrows indicate electron holes. (b) Illustrative schematic. N Si-V centers are placed in a phononic waveguide and the distance between two adjacent Si-V centers is fixed. Right shows the direction of the external magnetic field. (c) Si-V electronic structure under spin-orbit and Jahn-Teller interactions with and without an external magnetic field, and red arrows represent the transitions $|1\rangle \leftrightarrow |A\rangle$ and $|2\rangle \leftrightarrow |A\rangle$, coupled with Rabi frequencies Ω_{A1} and Ω_{A2} and detuning $\delta_1 + \delta$ and δ_1.

The unpaired electron of the ground state (excited state) of a single Si-V occupies one of the two degenerate orbital states, $|e_{gx}\rangle$ ($|e_{ux}\rangle$) and $|e_{gy}\rangle$ ($|e_{uy}\rangle$). Under the influence of spin-orbit interaction (the reasons for the form can be found in Appendix B) and the JT effect, the Hamiltonian in the $\{|e_{g(u)x} \uparrow\rangle, |e_{g(u),x} \downarrow\rangle, |e_{g(u),y} \uparrow\rangle, |e_{g(u),y} \downarrow\rangle\}$ basis can be written as

$$
\begin{aligned}
\hat{H}_{\text{or}} &= \hat{H}_{\text{SO}} + \hat{H}_{\text{JT}}, \\
&= -\lambda_{g,e} L_z S_z + \Upsilon_{g,e}^{\text{JT}}, \\
&= -\lambda_{g,e} \begin{bmatrix} 0 & i \\ -i & 0 \end{bmatrix} \otimes \frac{1}{2} \begin{bmatrix} 1 & 0 \\ 0 & -1 \end{bmatrix} + \begin{bmatrix} \Upsilon_x & \Upsilon_y \\ \Upsilon_y & -\Upsilon_x \end{bmatrix} \otimes I_2,
\end{aligned}
\tag{1}
$$

where $\lambda_{g,e}$ is the spin-orbit coupling [20]; Υ_x and Υ_y are the strengths of the JT coupling along x and y, respectively; and I_2 is the 2×2 identity matrix. In the case of $\Upsilon_{x,y} \ll \lambda_{g,e}$, diagonalizing $\hat{H}_{\text{or}}$, we can obtain the following eigenstates $\{|e_+, \uparrow\rangle, |e_-, \downarrow\rangle, |e_+, \downarrow\rangle, |e_-, \uparrow\rangle\}$, where $e_+ = -(1/\sqrt{2})(e_x + ie_y)$ and $e_- = (1/\sqrt{2})(e_x - ie_y)$ are the eigenstates of the angular momentum, L_z. Then, in the

presence of an external magnetic field with $B = 0.21$ T, the spin degeneracy can be lifted. The Hamiltonian of the Zeeman interaction can be denoted as

$$
\hat{H}_Z = f \gamma_L \mathbf{L} \cdot \mathbf{B} + \gamma_S \mathbf{S} \cdot \mathbf{B},
\tag{2}
$$

with $\gamma_L = \mu_B/\hbar$ and $\gamma_S = 2\mu_B/\hbar$ (μ_B is the Bohr magneton) are the orbital and spin gyromagnetic ratio, respectively; $\mathbf{B} = (B_x, B_y, B_z)$ is the magnetic field, $\mathbf{S} = (\hbar/2)(\sigma_x, \sigma_y, \sigma_z)$ is the spin operator; and f is the quenching factor, which only acts on γ_L due to dynamic JT coupling [103]. Solving the secular equation defined by $\hat{H}_{\text{or}} + \hat{H}_Z$, four eigenvectors $\{|0\rangle, |1\rangle, |2\rangle, |3\rangle\}$ for the ground state and four eigenvectors $\{|A\rangle, |B\rangle, |C\rangle, |D\rangle\}$ for the excited state can be calculated, as shown in Fig. 1(c).

$$
\begin{aligned}
|0\rangle &\approx |e_{g+} \searrow\rangle \equiv |e_{g+} \downarrow\rangle - \eta_+ |e_{g+} \uparrow\rangle, \\
|1\rangle &\approx |e_{g-} \nearrow\rangle \equiv |e_{g-} \uparrow\rangle - \eta_- |e_{g-} \downarrow\rangle, \\
|2\rangle &\approx |e_{g-} \searrow\rangle \equiv |e_{g-} \downarrow\rangle + \eta_- |e_{g-} \uparrow\rangle, \\
|3\rangle &\approx |e_{g+} \nearrow\rangle \equiv |e_{g+} \uparrow\rangle + \eta_+ |e_{g+} \downarrow\rangle, \\
|A\rangle &\approx |e_{u+} \searrow\rangle \equiv |e_{u+} \downarrow\rangle - \eta_+ |e_{u+} \uparrow\rangle, \\
|B\rangle &\approx |e_{u-} \nearrow\rangle \equiv |e_{u-} \uparrow\rangle - \eta_- |e_{u-} \downarrow\rangle, \\
|C\rangle &\approx |e_{u-} \searrow\rangle \equiv |e_{u-} \downarrow\rangle + \eta_- |e_{u-} \uparrow\rangle, \\
|D\rangle &\approx |e_{u+} \nearrow\rangle \equiv |e_{u+} \uparrow\rangle + \eta_+ |e_{u+} \downarrow\rangle,
\end{aligned}
$$

where $\eta_\pm = \frac{2 B_x \gamma_s}{-\lambda_{\text{SO}} \pm 2 B_z \gamma_s + \sqrt{\lambda_{\text{SO}}^2 \pm 4\lambda_{\text{SO}} B_z \gamma_s + 4(B_x^2 + B_z^2)\gamma_s^2}}$.

In the present system, only four ground states and the first excited state are considered. The Hamiltonian of a single Si-V center can be expressed as

$$
\hat{H}_{\text{Si-}V} = \sum_{i=0}^{3} \omega_i |i\rangle\langle i| + \omega_a |A\rangle\langle A|,
\tag{3}
$$

where ω_i and ω_A are the energies of the ground states, $|i\rangle$, and the excited state, $|A\rangle$.

We can find that each basis vector in the ground-state subspace contains spin-up and spin-down components when the magnetic field and Si-V axes are not oriented in the same direction, so the ground-state basis vectors can be coupled to all energy levels. We applied two lasers, coupling $|1\rangle \leftrightarrow |A\rangle$ and $|2\rangle \leftrightarrow |A\rangle$, with Rabi frequencies of Ω_{A1} and Ω_{A2} used simultaneously, and frequencies of ω_{A2} and ω_{A3}, respectively, as illustrated in Fig. 1(c). The driving Hamiltonian can be written as

$$
\hat{H}_d = \frac{\Omega_{A1}}{2} |A\rangle\langle 1| e^{i\omega_{A1} t} + \frac{\Omega_{A2}}{2} |A\rangle\langle 2| e^{i\omega_{A2} t} + \text{H.c.}
\tag{4}
$$

The detuning is $\delta_1 = \omega_a - \omega_{A2} - \omega_2 = \omega_a - \omega_{A1} - \delta$.

We consider N Si-V centers in a 1D phononic waveguide [see Fig. 1(b)], where the distance between two

adjacent Si-*V* centers is fixed, and the structure of the Si-*V* center is shown in Fig. 1(b). For the phonon waveguide, the cross section, A, is much larger than the length, L; the phonon modes can be modeled as elastic waves with a displacement field $\vec{u}(\vec{r}, t)$, obeying the equation of motion [23]:

$$\rho \frac{\partial^2}{\partial t^2} \vec{u} = (\lambda + \mu) \vec{\nabla}(\vec{\nabla} \cdot \vec{u}) + \mu \vec{\nabla}^2 \vec{u}, \tag{5}$$

where the Lamé constants are $\lambda = (\nu E / ((1 + \nu)(1 - 2\nu)))$ and $\mu = (E / (2(1 + \nu)))$; E is the Young's modulus; ν is the Poisson ratio; and ρ is the mass density. The equation of motion meets the periodic boundary condition, and the amplitudes $A_{n,k}(t)$ obey $\ddot{A}_{n,k}(t) + \omega_{n,k}^2(t) A_{n,k}(t) = 0$. The canonical coordinate, $Q_{n,k} = (A_{n,k} + A_{n,-k}^*)/\sqrt{2}$, and the canonical momenta, $P_{n,k}$, can be written as

$$Q_{n,k} = \sqrt{\frac{\hbar}{2M\omega_{n,k}}}(\hat{a}_{n,k}^\dagger + \hat{a}_{n,k}),$$

$$P_{n,k} = i\sqrt{\frac{\hbar M \omega_{n,k}}{2}}(a_{n,k}^\dagger + \hat{a}_{n,k}),$$

where $M = \rho A L$, and $\hat{a}_{j,k}$ ($\hat{a}_{j,k}^\dagger$) is the annihilation (creation) operator of the kth mode of the jth branch at a frequency of $\omega_{j,k}$. As for the strain coupling caused by the small displacement of the defect atoms, the interaction in the Born-Oppenheimer approximation [17,104] can be approximated as

$$\hat{H}_s = \sum_{n,j,k} g_{j,k,n} \hat{a}_{j,k} \hat{J}_+^n e^{ikx_n} + \text{H.c.}, \tag{6}$$

where $\hat{J}_- = \hat{J}_+^\dagger = |0\rangle\langle 2| + |1\rangle\langle 3|$ means the lowering operator of the kth mode of the jth branch of the nth Si-*V* center, $g_{j,k,n} = d\sqrt{(\hbar k^2/2\rho L A \omega_{j,k})}\xi_{j,k}(y_n, z_n)$ is the coupling strength, $d/2\pi = 1$ PHz is the strain sensitivity, $\xi_{n,k}(y_n, z_n)$ is the dimensionless coupling profile accounting for the specific strain distribution and for a homogeneous compression mode $\xi(y, z) = 1$, and x_n denotes the position of the nth Si-*V* center. So the Hamiltonian of the phonon modes can be described by

$$\hat{H}_{\text{ph}} = \sum_{j,k} \omega_{j,k} \hat{a}_{j,k}^\dagger \hat{a}_{j,k}. \tag{7}$$

Then, the full Hamiltonian of the system is

$$\hat{H}_{\text{full}} = \hat{H}_{\text{Si-}V} + \hat{H}_{\text{ph}} + \hat{H}_d + \hat{H}_s. \tag{8}$$

B. The effective Hamiltonian

In the interaction picture, by considering the rotating-wave approximation and using effective Hamiltonian theory [105,106] with the condition of $\delta_1, \delta \gg \Omega_{A2}, \Omega_{A3}$, the

Hamiltonian of the nth Si-*V* center can be rewritten as

$$\hat{H}_n(t) = g\hat{a}(|2\rangle_n\langle 0|e^{i\Delta_1 t} + |3\rangle_n\langle 1|e^{i\Delta_2 t})$$
$$+ \frac{\Omega}{2}|2\rangle_n\langle 1|e^{i\delta t} + \text{H.c.}, \tag{9}$$

where $\Omega = -\Omega_{A2}^* \Omega_{A3}(2\delta_1 + \delta)/4\delta_1(\delta_1 + \delta)$ [see Fig. 2]. We have dropped the Stark shift that can be compensated for by additional field-induced energy shifts [107,108].

Furthermore, in the condition of $\Delta_1, \Delta_2 \gg g, \Omega$, the effective Hamiltonian can be denoted as

$$\hat{H}_{n\text{eff}} = \frac{\Omega_{\text{eff}}}{2}\hat{a}^\dagger |0\rangle_n\langle 1|e^{i(\delta - \Delta_1)t} + \text{H.c.}, \tag{10}$$

with $\Omega_{\text{eff}} = -\Omega g(\Delta_1 + \delta)/2\Delta_1\delta$. We find that its form is consistent with the Jaynes-Cummings model that can be used to realize quantum computation [109].

Based on the effective Hamiltonian of the Si-*V*-center system in Eq. (10), we propose to construct logic gates with Si-*V* centers placed in the 1D phononic waveguide. For simplicity, we consider the single-excitation mode and regard $|10\rangle$ and $|01\rangle$ as logical qubits $|0\rangle_L$ and $|1\rangle_L$. $|10\rangle$ ($|01\rangle$) is the abbreviation $|1\rangle \otimes |0\rangle$ ($|0\rangle \otimes |1\rangle$), where the first ket in the product is the Fock state of the phonon, and the second is the energy level of the Si-*V* center. The effective Hamiltonian Eq. (10) can be written as

$$\hat{H}_1 = \frac{|\Omega_{\text{eff}}|}{2} \begin{pmatrix} 0 & e^{i\varphi} \\ e^{-i\varphi} & 0 \end{pmatrix}, \tag{11}$$

where $|\Omega_{\text{eff}}|$ and φ denote the amplitude and phase of Ω_{eff}, respectively. The degree of conformity between the Hamiltonians in Eqs. (8) and (10) is shown in Fig. 3(a). It can be seen that the effective Hamiltonian and the full
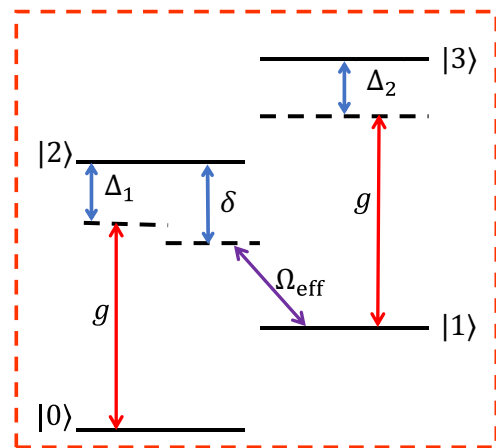

FIG. 2. Effective energy-level-coupling structure, where g is the coupling strength of the strain; Ω_{eff} is the effective coupling strength of $|1\rangle \leftrightarrow |2\rangle$; the condition of Δ_1, Δ_2, and δ is the detuning of $|0\rangle \leftrightarrow |2\rangle$, $|1\rangle \leftrightarrow |3\rangle$, and $|1\rangle \leftrightarrow |2\rangle$, respectively.
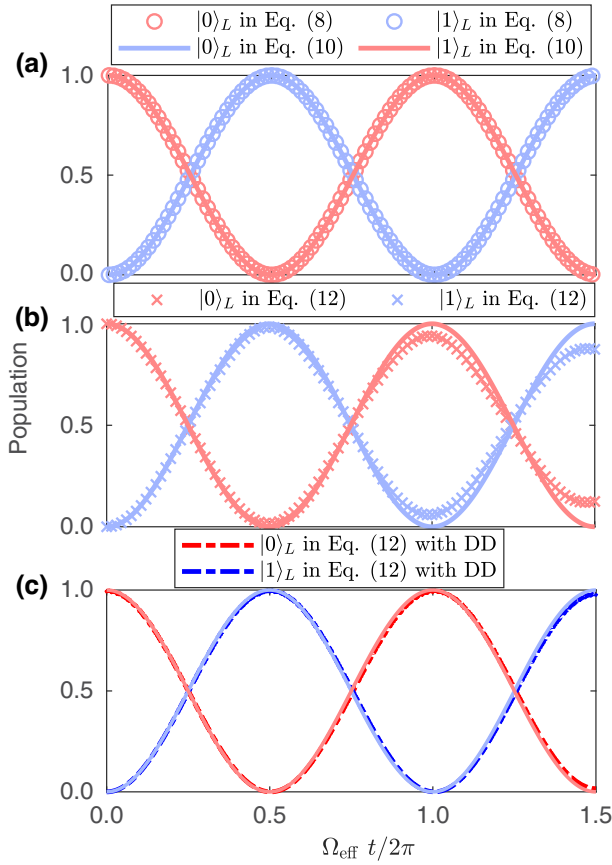
FIG. 3. (a) Comparison of the population of $|0\rangle_L$ and $|1\rangle_L$ from Eq. (8) with that from Eq. (10). (b),(c) Comparison of the population of $|0\rangle_L$ and $|1\rangle_L$ from Eq. (10) with that from Eq. (12) without and with DD protection, respectively, where $\Omega/2\pi = 10$ MHz, $g/2\pi = 5$ MHz, $\Delta_1/2\pi = 100$ MHz, $\Delta_2/2\pi = 500$ MHz, and $\delta = \Delta_1$.

Hamiltonian agree with each other very well. All theories hereafter are based on the effective Hamiltonian, and all numerical simulations are based on the original Hamiltonian.

For the quantum system considered here, we consider it to be coupled to environment E, so the total Hamiltonian is

$$\hat{H} = \hat{H}_1 \otimes \mathbb{I}_E + \mathbb{I}_S \otimes \hat{H}_E + \hat{H}_I, \qquad (12)$$

where $\mathbb{I}$ is the identity operator, $\hat{H}_E$ includes all environment terms, and $\hat{H}_I$ is the interaction between qubits and the environment. The dominant environment of the Si-V electron spin is a nuclear spin bath formed by the ^{13}C isotope with the nuclear-spin quantum number $I = 1/2$, which has 1.1% abundance [110], and the nuclear-spin quantum number of other C isotopes is 0. In the Si-V center, the electron wave function is localized around the vacancy site, which only extends to several angstroms. The interaction between nuclear spins within this range through the dipole-dipole interaction is

$$\hat{H}_{\text{dip}} = \sum_{i<j} D_{ij} [\mathbf{I}_i \cdot \mathbf{I}_j - \frac{3(\mathbf{I}_i \cdot \mathbf{r}_{i,j})(\mathbf{r}_{i,j} \cdot \mathbf{I}_j)}{r_{ij}^2}], \qquad (13)$$

where $\mathbf{r}_{ij}$ is the displacement from the ith to the jth nuclear spin; $D_{ij} = \mu_0 \gamma_n^2/(4\pi r_{ij}^3)$, where μ_0 is the vacuum permeability and $\gamma_n = 6.73 \times 10^7$ (rad/s)/T is the gyromagnetic ratio of the ^{13}C nuclear spins. The interaction between the system and environment is coupled through the hyperfine interaction, which can be represented as

$$\hat{H}_I = \sum_i \sigma \cdot \mathbb{A}_i \cdot \mathbf{I}_i, \qquad (14)$$

where

$$\mathbb{A}_i = \frac{\mu_0 \gamma_e \gamma_n}{r_{iv}^3} \left(1 - \frac{3 \mathbf{r}_{iv} \mathbf{r}_{iv}}{r_{iv}^2} \right),$$

$\sigma = (\sigma_x, \sigma_y, \sigma_z)$, $\mathbf{r}_{iv}$ is the displacement of the ith ^{13}C nuclear spin from the Si-V center site, and $\gamma_e = -1.76 \times 10^{11}$ rad/s/T is the gyromagnetic ratio of the electron. The relationship between the strength of the hyperfine interaction and the mean decoherence time is $T_2^* \equiv \sqrt{8}/\sum_i \mathbb{A}_i$ [111]. The mean decoherence time of the Si-V center is $T_2^* = 216$ μs at 40 mK [102].

Accordingly, we simulated the impact of the environment on system evolution. From Fig. 3(b), we can see that, with an increase of time, the environment has an increasingly significant impact on the system. Fortunately, as described in Appendix C, after applying a concatenated dynamical decoupling (CDD) pulse sequence, the evolution operator of the total Hamiltonian, $\hat{H}$, is

$$
\begin{aligned}
\hat{U}_{\text{tot}}(\tau) &= \left[Z \, e^{-i \int_{3\tau/4}^{\tau} \hat{H} \, dt} \, Z \cdot Y e^{-i \int_{\tau/2}^{3\tau/4} \hat{H} \, dt} \, Y \cdot X \, e^{-i \int_{\tau/4}^{3\tau/4} \hat{H} \, dt} \, X \cdot e^{-i \int_0^{\tau/4} \hat{H} \, dt} \right] \\
&= e^{-i \left[Z \int_{3\tau/4}^{\tau} \hat{H}_1 \, dt \, Z + Z \int_{3\tau/4}^{\tau} \hat{H}_I \, dt \, Z + \hat{H}_E \tau/4 \right]} \cdot e^{-i \left[Y \int_{\tau/2}^{3\tau/4} \hat{H}_1 \, dt \, Y + Y \int_{\tau/2}^{3\tau/4} \hat{H}_I \, dt \, Y + \hat{H}_E \tau/4 \right]} \\
&\quad \cdot e^{-i \left[X \int_{\tau/4}^{\tau/2} \hat{H}_1 \, dt \, X + X \int_{\tau/4}^{\tau/2} \hat{H}_I \, dt \, X + \hat{H}_E \tau/4 \right]} \cdot e^{-i \left[\int_0^{\tau/4} (\hat{H}_1 + \hat{H}_I + \hat{H}_E) \, dt \right]} \\
&= e^{-i \left(\hat{H}_E \tau + \int_0^{\tau} \hat{H}_1 \, dt \right) + \mathcal{O}(\tau^2)} \\
&= U_1(\tau) \otimes U_E(\tau) + \mathcal{O}(\tau^2). \qquad (15)
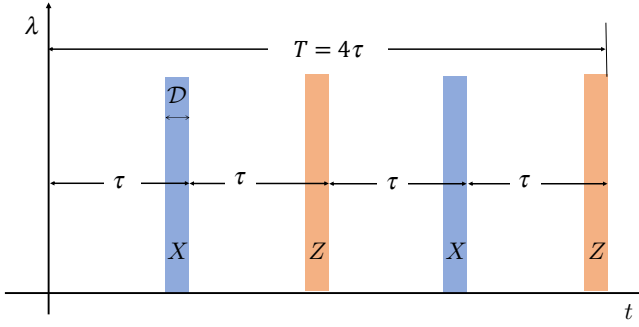\end{aligned}
$$

FIG. 4. Schematic diagram of CDD pulses, where T is the total evolution time; τ is the interval of each decoupling pulse; and $\mathcal{D}$ and λ are the duration and strength of each decoupling pulse, respectively.

That is to say, the effect of the environment can be eliminated approximately after adding the CDD pulse sequence, as shown in Fig. 3(c), which proves that DD is an effective method for protecting system coherence.

Inspired by this, we consider adding the CDD pulse sequence shown in Fig. 4 and periodic DD k-times (PDD$_k$) sequences to the system to further improve the performance of the gate. Multiple fast and strong pulses with a pulse area of $\pi/2$ are applied, which can remove the impact of the environment to a great extent (details are presented in Appendix C). A schematic diagram of the evolution trajectory with the impact of the environment and decoupled pulses is shown in Fig. 5(b). Because of the effect of the environment, the trajectory of the evolution state will have a slight deviation from the ideal situation shown in Fig. 5(a). This deviation can be eliminated by the DD pulses (represented by orange and blue arrows with solid lines), so as to achieve the ideal evolution. Consequently, the decoherence caused by the interaction between the quantum system and environment can be inhibited greatly.
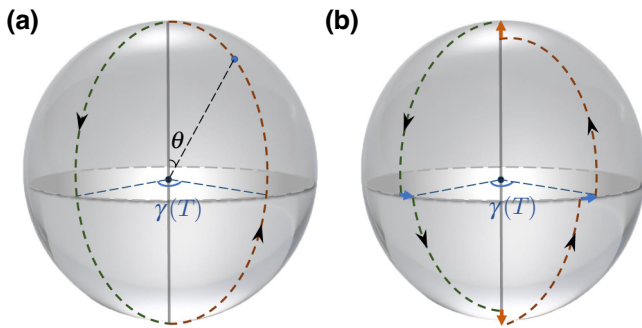

FIG. 5. Evolution paths for the single-loop NGQC scheme (a) without and (b) with the impact of the environment and decoupled pulses (taking the basic pulse as an example).

III. IMPLEMENTATION

By combining a set of universal single-qubit gates and a nontrivial two-qubit gate, universal quantum computation can be realized [112]. In this section, we show how to use Si-V centers to realize general DD-protected nonadiabatic geometric quantum logic gates.

A. Geometric single-qubit gates

To construct general single-qubit gates, we choose a pair of orthogonal auxiliary bases:

$$
\begin{aligned}
|\varphi_1(t)\rangle &= \sin\frac{\theta(t)}{2}e^{-i\phi(t)}|0\rangle_L - \cos\frac{\theta(t)}{2}|1\rangle_L, \\
|\varphi_2(t)\rangle &= \cos\frac{\theta(t)}{2}|0\rangle_L + \sin\frac{\theta(t)}{2}e^{i\phi(t)}|1\rangle_L.
\end{aligned}
\tag{16}
$$

Then, we have $\Omega_{\text{eff}}(t) = ie^{i\phi(t)}[\dot{\theta}(t) + i\cos\theta(t)\sin\theta(t)\dot{\phi}(t)]$ and $\Delta_{\text{eff}}(t) = -\frac{1}{2}\sin^2\theta(t)\dot{\phi}(t)$, where $\Delta_{\text{eff}} = \delta - \Delta_1$ (details are presented in Appendix D).

We take a single-qubit phase gate and a Hadamard gate as examples. For the phase gate, the polar angle, $\theta(t)$, and the azimuth angle, $\phi(t)$, vary by starting from the north pole $[\theta(0) = 0, \phi(0)]$, passing through the south pole, experiencing a sudden change $[\theta(t) = \pi, \phi(t) = \phi(0) + \pi/2]$, and finally returning to the north pole. Parameters in the Hamiltonian are

$$
\begin{cases}
\int_0^{T_1}\dot{\theta}(t)\,dt = \pi, & \phi(t) = 0, & t \in [0, T_1], \\
\int_{T_1}^{T}\dot{\theta}(t)\,dt = \pi, & \phi(t) = \pi/4, & t \in (T_1, T].
\end{cases}
\tag{17}
$$

A schematic diagram of the evolution path is shown in Fig. 5(a). The shapes of Ω and φ are shown in Fig. 6(a); these are easily achieved in experiments.

For the Hadamard gate (ignoring the global phase), the polar angle and the azimuth angle start from $[\theta(0) = (\pi/2), \phi(0) = \pi/2]$, passing the south pole and the north pole and back to the starting point. The parameters in the Hamiltonian satisfy

$$
\begin{aligned}
\int_0^{T_1}\dot{\theta}(t)\,dt &= \theta(0), & \phi(t) &= \pi/2, & t &\in [0, T_1], \\
\int_{T_1}^{T_2}\dot{\theta}(t)\,dt &= \pi, & \phi(t) &= \phi(0) - \frac{\pi}{4}, & t &\in (T_1, T_2], \\
\int_{T_2}^{T}\dot{\theta}(t)\,dt &= \pi - \theta(0), & \phi(t) &= \pi/2, & t &\in (T_2, T].
\end{aligned}
\tag{18}
$$

We use the average fidelity, $\mathcal{F}$, of an alterable initial state $|\psi(0)\rangle = \cos\theta|0\rangle_L + \sin\theta|1\rangle_L$, and the fidelity, F, which is defined as

$$
\mathcal{F} = \frac{1}{2\pi}\int_0^{2\pi}\langle\psi_{\text{ideal}}|\rho(T)|\psi_{\text{ideal}}\rangle\,d\theta,
\tag{19a}
$$

$$
F = \langle\psi_{\text{ideal}}|\rho(T)|\psi_{\text{ideal}}\rangle,
\tag{19b}
$$

to evaluate the performance of the gate, where $|\psi_{\text{ideal}}\rangle = U(T)|\psi(0)\rangle$ is the ideal state and ρ is the density matrix.
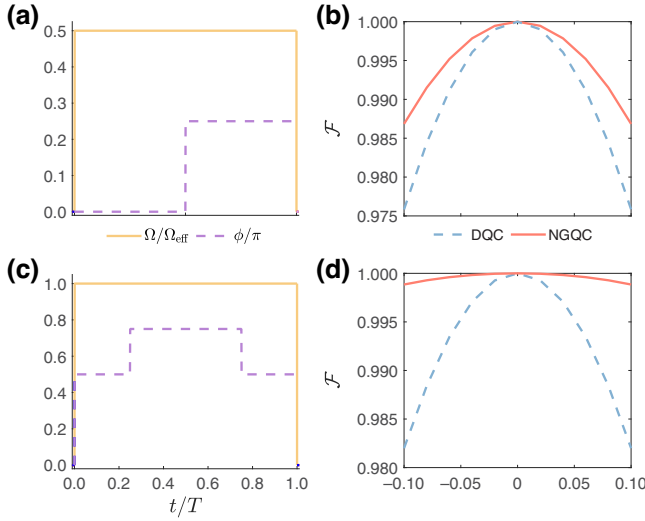
FIG. 6. Numerical simulation of the phase gate and the Hadamard gate. Shapes of Ω and ϕ for the phase gate (a) and the Hadamard gate (c). Average fidelity, $\mathcal{F}$, of the phase gate (b) and the Hadamard gate (d) against control error.

According to Ref. [113], the Liouville equation, $\dot{\rho}_{\mathrm{tol}}(t) = -i[\hat{H}(t), \rho_{\mathrm{tol}}(t)]$, can be used to calculate the density matrix. The density operator is $\rho(t) = \mathrm{Tr}_E \rho_{\mathrm{tol}}(t)$. The evolution operator of the phase (Hadamard) gate is described as $U(T) = \exp(-i\pi\sigma_z/2)$ $[U(T) = \exp(-i\pi\sigma_x/4)]$.

In practical operations, there will inevitably be some fluctuations in the control pulse, which means that the control pulse, $\Omega \to (1 + \epsilon)\Omega$, within the range $\epsilon \in [-0.1, 0.1]$—the method of geometric evolution—can effectively suppress this error. To demonstrate the robustness of the geometric phase, we compare the robustness of our scheme against Rabi error with the dynamical quantum computation (DQC) scheme (the implementation of DQC is shown in Appendix F), and we do not consider the influence of the environment in the discussion on robustness. The red solid line and the blue dashed line represent the average fidelity of NGQC and DQC varying control error ϵ, respectively. We find that the geometric gates can surpass dynamical gates from Figs. 6(b) and 6(d). To better illustrate the impact of parameter fluctuations on fidelity, we provide an analytical solution for fidelity with parameter fluctuations ϵ in Appendix E. Although different fidelity-solving methods may lead to slight deviations, the impact of control-parameter fluctuations on fidelity can be clearly explained.

For decoherence caused by the environment, the fidelity, F, defined in Eq. (19b) of the phase gate and Hadarmard gate without DD and with various DD pulses are shown in Fig. 7 (assuming the initial state is in $|0\rangle_L$); different color bars represent the average fidelity achievable by different DD pulses. We find that, as the pulse period increases, the average fidelity becomes higher and higher. After applying
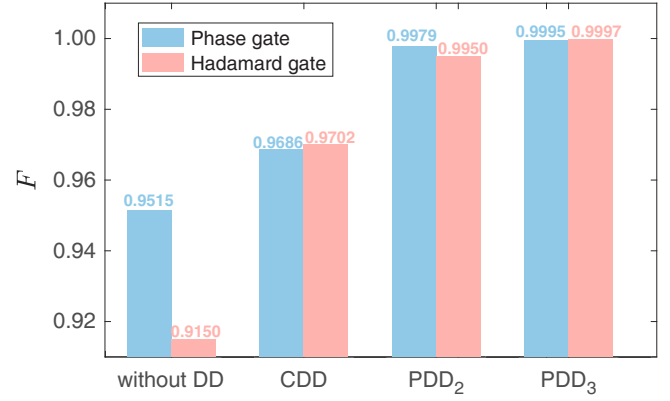

FIG. 7. Fidelity of the phase gate and the Hadamard gate based on the conditions in Eqs. (17) and (18) without DD and with CDD sequences, PDD$_2$ sequences, and PDD$_3$ sequences, respectively. Control parameters are the same as those in Fig. 3.

CDD, PDD$_2$, and PDD$_3$, the fidelity of the phase gate (Hadamard gate) reaches 0.9702 (0.9686), 0.995 (0.9979), and 0.9997 (0.9995), respectively.

We further demonstrate the robustness of our scheme against the effect of environment, $\sum_i \mathbb{A}_i \to (1 + \eta) \sum_i \mathbb{A}_i$. The robustness of the phase gate (Hadamard gate) changing with the strength of the environmental interaction is shown in Figs. 8(a) and 8(b). To more clearly demonstrate the impact of different decoupling pulse sequences on average fidelity, we selected the y axis as the natural logarithmic form. From Fig. 8, we can see that the
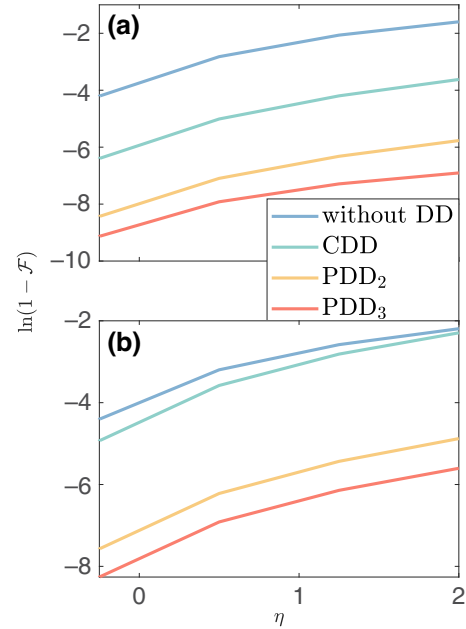

FIG. 8. Robustness of (a) the phase gate and (b) the Hadamard gate upon varying the strength of environmental interaction, η. Control parameters are the same as those in Fig. 3.

DD greatly protects the nonadiabatic geometric quantum gates from environment-induced decoherence. We provide a quantitative analysis in Appendix G, regarding the reason why fidelity decreases with increasing interaction strength between the system and environment. Moreover, from Eq. (15), we can see that DD pulses can eliminate the first-order term of the interaction, while higher-order terms still have a reducing effect on the fidelity of the system. The more DD pulse sequences are added, the further their higher-order terms can be eliminated. However, as the intensity of the interaction increases, the fidelity still decreases.

B. Nontrivial geometric two-qubit gate

In this section, we demonstrate the construction of the nontrivial two-qubit geometric gate using Si-V centers. Here, we consider two Si-V centers in the phononic waveguide and define the effective detuning, $\delta - \Delta_1 = \Lambda_1$. The Hamiltonian becomes

$$\hat{H}_n = \frac{\Omega_{\text{eff}}}{2}\hat{a}^\dagger |0\rangle_n \langle 1| e^{i\Lambda_n t} + \text{H.c.}, \tag{20}$$

for the nth Si-V center coupled to the phononic waveguide. When $\Lambda_n \gg \Omega_{\text{eff}}$, the effective Hamiltonian of the system can be written as

$$\hat{H}_2 = -\Omega_{\text{eff}}^2 \frac{\Lambda_1 + \Lambda_2}{8\Lambda_1\Lambda_2}\hat{\sigma}_1^-\hat{\sigma}_2^+ e^{i(\Lambda_1-\Lambda_2)t} + \text{H.c.}, \tag{21}$$

where $\hat{\sigma}_1^-$ ($\hat{\sigma}_2^+$) denotes the energy-level decline (rise) operator of the first (second) Si-V center. Now, similar to the single-qubit gate, we encode $|0\rangle_{\text{Si-}V}$ ($|1\rangle_{\text{Si-}V}$) as logical qubit $|0\rangle_L$ ($|1\rangle_L$), so the Hamiltonian in Eq. (21) can be written in the following form in the basis space $\{|00\rangle_L |01\rangle_L |10\rangle_L |11\rangle_L\}$:

$$\hat{H}_2 = - \begin{pmatrix} 0 & 0 & 0 & 0 \\ 0 & \Lambda_2 - \Lambda_1 & \dfrac{\Omega_{\text{eff}}^2(\Lambda_1 + \Lambda_2)}{8\Lambda_1\Lambda_2} & 0 \\ 0 & \dfrac{\Omega_{\text{eff}}^2(\Lambda_1 + \Lambda_2)}{8\Lambda_1\Lambda_2} & \Lambda_1 - \Lambda_2 & 0 \\ 0 & 0 & 0 & 0 \end{pmatrix}. \tag{22}$$

Similar to the single-qubit case, we choose four auxiliary bases

$$|\varphi_1(t)\rangle = |00\rangle_L,$$

$$|\varphi_2(t)\rangle = \cos\frac{\theta(t)}{2}|01\rangle_L + \sin\frac{\theta(t)}{2}e^{i\phi(t)}|10\rangle_L,$$

$$|\varphi_3(t)\rangle = \sin\frac{\theta(t)}{2}e^{-i\phi(t)}|01\rangle_L - \cos\frac{\theta(t)}{2}|10\rangle_L,$$

$$|\varphi_4(t)\rangle = |11\rangle_L. \tag{23}$$

Then, we have $O_{\text{eff}} \equiv \Omega_{\text{eff}}^2((\Lambda_1 + \Lambda_2)/4\Lambda_1\Lambda_2) = ie^{i\phi(t)}[\dot{\theta}(t) + i\cos\theta(t)\sin\theta(t)\dot{\phi}(t)]$ and $\Lambda_{\text{eff}}(t) = \frac{1}{2}\sin^2\theta(t)\dot{\phi}(t)$, where $\Lambda_{\text{eff}} = \Lambda_2 - \Lambda_1$ (details are presented in Appendix D).

Here, we choose $\Lambda_1 = \Lambda_2$, $\gamma(T) = \pi/2$, $\theta(0) = \pi/2$, and $\varphi(0) = \pi$; the parameters in the Hamiltonian are

$$\begin{array}{lll} \int_0^{T_1} O_{\text{eff}}\, dt = \theta(0), & \phi(t) = \pi, & t \in [0, T_1], \\ \int_{T_1}^{T_2} O_{\text{eff}}\, dt = \pi, & \phi(t) = \pi + \frac{\pi}{2}, & t \in (T_1, T_2], \\ \int_{T_2}^{T} O_{\text{eff}}\, dt = \pi - \theta(0), & \phi(t) = \pi, & t \in (T_2, T]. \end{array} \tag{24}$$

The azimuth angle, ϕ, changes twice at the south pole and north pole, so an *i*SWAP gate can be achieved, which is a universal gate for quantum computation [114].

The system Hamiltonian is $\hat{H}_2(t)$ in Eq. (9), and the interaction Hamiltonian is described as $\hat{H}_{I2(t)} = \sum_{\alpha=x,y,z}(\sigma_1^\alpha \otimes E_1^\alpha + \sigma_2^\alpha \otimes E_2^\alpha)$. The form of E_i is the same as the single-qubit case, which means that we assume each physical qubit has the same environment. Therefore, the DD pulse sequences play a role by applying each qubit. Then, we plot the fidelity of the *i*SWAP gate. The parameters are the same as those described in Sec. III A.

Similar to the single-qubit case, we consider that each environmental noise has fluctuations of η. The initial state is set as $|01\rangle_L$ for simplicity, and the fidelity, F, defined by Eq. (19b) is shown in Fig. 3. Furthermore, we introduce the DD sequences shown in Fig. 4 and PDD$_2$ and PDD$_3$ to improve the performance of the *i*SWAP gate. From the results of numerical simulations, one can see that the DD technique can protect the quantum system from decoherence and dephasing coming from the environment. The fidelity of the *i*SWAP gate varying with η is shown in Fig. 9, which shows the robustness of DD sequences.
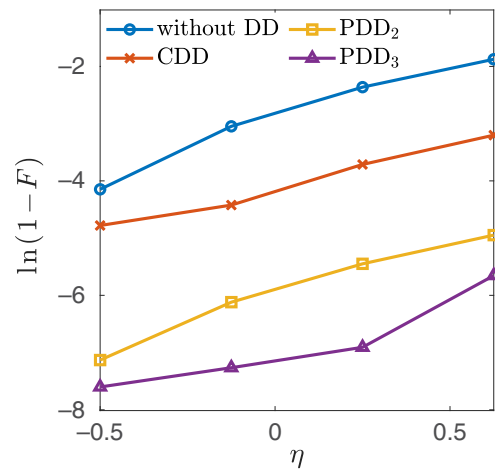

FIG. 9. Fidelity of the proposed *i*SWAP gate with the Si-V center varying with the strength of environment interaction η. Control parameters are set the same as Fig. 3.

IV. EXPERIMENTAL FEASIBILITY

In our scheme, the considered Si-V centers are coupled by a phononic waveguide. For state-of-the-art techniques, Si-V-center arrays can be assembled successfully [115], so as to implement the experimental structure. For the phonon waveguide, one can assume that the length is $L = 80$ μm, the cross section is $A = 80 \times 80$ nm^2, the Young's modulus is $E = 1050$ GPa, the Poisson ratio is $\nu = 0.2$, the mass density is $\rho = 3500$ kg/m^3 [23], and the resulting coupling strength is $g/2\pi \approx 5$ MHz. The condition of the single-excitation mode of a phonon can be satisfied when the temperature, T_e, is below 100 mK [102]. In numerical simulations, we selected a temperature of $T_e = 40$ mK, a mean decoherence time of the Si-V center of $T_2^* = 216$ μs, and duration of single-qubit logic gates of $2\pi/\Omega_{\text{eff}} = 2$ μs. The Rabi frequency of each decoupling pulse is chosen to be $\lambda = 2\pi \times 4$ MHz; the parameters in Fig. 4 are $\mathcal{D} = \pi/2/\lambda = 62.5$ ns, $\tau = 0.5$ μs, and $T = 2$ μs. Therefore, the relevant parameters of our scheme could be feasible in experiments.

V. CONCLUSION

We have proposed the implementation of Si-V centers in quantum computation with universal nonadiabatic geometric quantum gates. Dynamical decoupling pulse sequences are used to improve the immunity of the quantum system to environmental impact. Scalability can be achieved by a 1D phononic waveguide. Besides the scalability, our scheme is easy to initialize and read out. In addition, logical states of qubits are encoded in long-lifetime ground states of Si-V centers, which can reduce the effect of decoherence caused by spontaneous emission. In summary, our scheme can protect quantum gates from both the control error caused by actual operation due to the intrinsic robustness of geometric quantum logic gates and dephasing caused by the environment; these are two obstacles to the realization of high-fidelity quantum logic gates. Therefore, our scheme may provide a significant reference and alternative path for implementing high-fidelity geometric quantum computation in solid-state systems.

ACKNOWLEDGMENTS

APPENDIX A: THE JT EFFECT

In 1937, Jahn *et al.* proved that a molecule in an orbitally degenerate electronic state would be inherently unstable with respect to distortions of its nuclear configuration, which lowered the orbital symmetry [100]. The electrons have considerably smaller masses than the nuclei, and the motion of the nuclei adiabatically follows the Born-Oppenheimer approximation [116]. Therefore, the state function can be written as the product of the electronic wave function. Electrons move on the effective potential surface generated by the nuclei. A simple case is considered here: there is a mode with normal coordinate, Q, coupled to an electronic state that has twofold degeneracy. Then the potential energy caused by the JT interaction can be written as

$$\hat{H}_{\text{JT}}^Q = \frac{1}{2}Q^2 + F\begin{bmatrix} Q & 0 \\ 0 & -Q \end{bmatrix}. \tag{A1}$$

The first term is the vibronic potential of the nucleus, and F is the strength of the JT coupling. We consider linear JT coupling and $\Upsilon_{x,y} = FQ_{x,y}$. The harmonic potential, $\frac{1}{2}Q^2$, can be dropped because it acts equally on all states, that is, it causes a global energy shift. So, in the $\{|e_{g(e),x}\rangle, |e_{g(e),y}\rangle\}$ basis of Si-V-center states, the JT interaction Hamiltonian is

$$\hat{H}_{\text{JT}} = \begin{bmatrix} \Upsilon_x & \Upsilon_y \\ \Upsilon_y & -\Upsilon_x \end{bmatrix}. \tag{A2}$$

APPENDIX B: THE FORM OF $\hat{L}_z$

We already know the matrix elements of $\hat{L}_z$ in the $\{|e_+\rangle, |e_-\rangle\}$ (where we omit the subscripts g, u) basis is

$$\begin{bmatrix} 1 & 0 \\ 0 & -1 \end{bmatrix}. \tag{B1}$$

The transformation matrix between $\{|e_+\rangle, |e_-\rangle\}$ and $\{|e_x\rangle, |e_y\rangle\}$ is

$$\begin{pmatrix} |e_+\rangle \\ |e_-\rangle \end{pmatrix} = \begin{bmatrix} -1 & -i \\ 1 & i \end{bmatrix}\begin{pmatrix} e_x \\ e_y \end{pmatrix}. \tag{B2}$$

Therefore, in the basis of $\{|e_x\rangle, |e_y\rangle\}$, the $\hat{L}_z$ is

$$\begin{bmatrix} 0 & i \\ -i & 0 \end{bmatrix}. \tag{B3}$$

We define the ladder operators $\hat{L}_\pm = \hat{L}_x \pm i\hat{L}_y$ and find that $\hat{L}_\pm Y_l^{ml} = \hbar\sqrt{(l \mp m_l)(l \pm m_l + 1)}Y_l^{m\pm1}$, which means $\hat{L}_\pm$ does not cause any direct coupling between e_+ and e_-. Consequently, all matrix elements of $\hat{L}_{x(y)}$ in the $\{|e_x\rangle, |e_y\rangle\}$ basis are zero.

APPENDIX C: UNIVERSAL DYNAMICAL DECOUPLING PULSE SEQUENCES

In the process of gate implementation, evolution is inevitably influenced by the surrounding environment, which can lead to a reduction of fidelity. Here, a set of general pulse sequences that can cancel out the system and environment are derived. First, for open quantum systems, we consider the total Hamiltonian $\hat{H} = \hat{H}_s + \hat{H}_e + \hat{H}_{se}$, where $\hat{H}_s$ and $\hat{H}_e$ contain only terms acting on the system or environment, and the system-environment coupling Hamiltonian of the most general single qubit is written as [81,83,84]

$$\hat{H}_{se} = \hat{H}_s \otimes \hat{H}_e = \sigma \cdot \mathbf{E}, \qquad (C1)$$

where $\sigma = (\sigma_x, \sigma_y, \sigma_z)$ denotes the system Hamiltonian and $\mathbf{E} = (E_x, E_y, E_z)$ expresses the environment operator. The unwanted noise induced by the open system originated from the Hamiltonian $\hat{H}_{se}$. The unwanted evolution operator can be expressed as $f_\tau = e^{-i\tau \hat{H}_{se}}$. DD strategies specifically aimed to eliminate the impact of $\hat{H}_{se}$. First, we apply two X pulses that last for a period of time $\mathcal{D}$ with strength λ, and $\mathcal{D}\lambda = (\pi/2)$, i.e., $X = e^{i\mathcal{D}\lambda\sigma^x} \otimes I_B = e^{-i(\pi/2)\sigma^x} \otimes I_B = -i\sigma^x \otimes I_B$ on the system. When $\mathcal{D} \to 0$, $\lambda \to \infty$, the condition $\mathcal{D}\lambda = (\pi/2)$ can be satisfied. Then, the unwanted evolution can be expressed as

$$Xf'_{2\tau} = Xf_\tau Xf_\tau = e^{-2i\tau(\sigma^x \otimes B^x + H_e)} + \mathcal{O}(\tau^2), \qquad (C2)$$

which means that the $Xf_\tau Xf_\tau$ pulse sequence can cancel out both the y and z contributions from the environment. Then we apply the Y pulse, $Y = e^{i\mathcal{D}\lambda\sigma^y} \otimes I_B = e^{-i(\pi/2)\sigma^y} \otimes I_B = -i\sigma^y \otimes I_B$, on the system,

$$\begin{aligned} Yf'_{2\tau}Yf'_{2\tau} &= YXf_\tau Xf_\tau YXf_\tau Xf_\tau, \\ &= Zf_\tau Xf_\tau Zf_\tau Xf_\tau, \\ &= e^{-i4\tau\hat{H}_e} + \mathcal{O}(\tau^2). \end{aligned} \qquad (C3)$$

So, when the evolution time is $t = 4\tau$, the system can decouple from the environment, that is, *ZXZX* pulse sequences are universal decoupling pulse sequences that can reduce the impact of the environment on the system. We call this universal decoupling sequence, *ZXZX*, a CDD pulse sequence. Here, we can repeat the CDD pulse sequence periodically k times (PDD$_k$) [86] to further enhance the performance of the system. We have

$$Zf_\tau Xf_\tau Zf_\tau Xf_\tau = (Zf_\tau Z)(Yf_\tau Y)(Xf_\tau X)(If_\tau I). \qquad (C4)$$

The decoupling group constituted by elements $\{I, X, Y, Z\}$ can achieve our decoupling goal (ignoring the global phase).

For the two-qubit case, the system-environment interaction can be written as

$$\hat{H}_{se} = \sum_{\alpha=x,y,z} \sum_{i=1,2} \sigma_i^\alpha \otimes E_i^\alpha, \qquad (C5)$$

which means each qubit interacts with its environment. The three-body interaction, $\sigma_{i_1}^{\alpha_1}\sigma_{i_2}^{\alpha_2} \otimes E_{i_1 i_2}^{\alpha_1 \alpha_2}$, can be neglected because it is much weaker. The decoupling group can be selected as $\{I^{\otimes 2}, X^{\otimes 2}, Y^{\otimes 2}, Z^{\otimes 2}\}$, that is, adding the same decoupling sequences to each qubit.

APPENDIX D: NONADIABATIC GEOMETRIC HAMILTONIAN

Here, we use the reverse-engineering scheme to give the target Hamiltonian for a system satisfying nonadiabatic geometric conditions [54]. For the single-qubit case, the orthogonal auxiliary bases can be chosen as

$$\begin{aligned} |\varphi_1(t)\rangle &= \sin\frac{\theta(t)}{2}e^{-i\phi(t)}|0\rangle - \cos\frac{\theta(t)}{2}|1\rangle, \\ |\varphi_2(t)\rangle &= \cos\frac{\theta(t)}{2}|0\rangle + \sin\frac{\theta(t)}{2}e^{i\phi(t)}|1\rangle, \end{aligned} \qquad (D1)$$

where $|0\rangle$ and $|1\rangle$ are two logical states of a qubit, and $\theta(t)$ and $\phi(t)$ are the time-dependent parameters. Then, the Hamiltonian of the system can be expressed as

$$\begin{aligned} \hat{H}(t) &= i\sum_{k \neq l}^{2} \langle\varphi_l(t)|\dot{\varphi}_k(t)\rangle|\varphi_l(t)\rangle\langle\varphi_k(t)|, \\ &= \Delta(t)(|1\rangle\langle 1| - |0\rangle\langle 0|) + \left[\frac{\Omega(t)}{2}|1\rangle\langle 0| + \text{H.c.}\right]. \end{aligned} \qquad (D2)$$

Then, we have $\Omega(t) = ie^{i\phi(t)}[\dot{\theta}(t) + i\cos\theta(t)\sin\theta(t)\dot{\phi}(t)]$ and $\Delta(t) = -\frac{1}{2}\sin^2\theta(t)\dot{\phi}(t)$.

Corresponding to the auxiliary basis vectors, the initial states of the system are

$$\begin{aligned} |\psi_1(0)\rangle &= |\varphi_1(0)\rangle = \sin\frac{\theta(0)}{2}e^{-i\phi(0)}|0\rangle - \cos\frac{\theta(0)}{2}|1\rangle, \\ |\psi_2(0)\rangle &= |\varphi_2(0)\rangle = \cos\frac{\theta(0)}{2}|0\rangle + \sin\frac{\theta(0)}{2}e^{i\phi(0)}|1\rangle. \end{aligned} \qquad (D3)$$

After a cyclic evolution, the evolution operator can be written as

$$U(T) = e^{-i\gamma(T)}|\psi_1(0)\rangle\langle\psi_1(0)| + e^{i\gamma(T)}|\psi_2(0)\rangle\langle\psi_2(0)|,$$

$$= \begin{pmatrix} \cos\gamma(T) + i\cos\theta_0\sin\gamma(T) & ie^{-i\phi_0}\sin\gamma(T)\sin\theta_0 \\ ie^{i\phi_0}\sin\gamma(T)\sin\theta_0 & \cos\gamma(T) - i\cos\theta_0\sin\gamma(T) \end{pmatrix},$$

$$= e^{-i\gamma(T)\mathbf{n}\cdot\sigma}, \tag{D4}$$

where $\theta_0 \equiv \theta(0)$, $\phi_0 \equiv \phi(0)$, and $\gamma(T) = i\int_0^T\langle\varphi_1(t)|\dot{\varphi}_1(t)\rangle dt = -i\int_0^T\langle\varphi_2(t)|\dot{\varphi}_2(t)\rangle dt = \frac{1}{2}\int_0^T[1 - \cos\theta(t)\dot{\phi}(t)]dt = \frac{1}{2}\oint_C[1 - \cos\theta(t)]d\phi$. It can be clearly seen that $\gamma(T)$ is half of the solid angle, independent of the evolution details, and $\mathbf{n} = [\sin\theta(0)\cos\phi(0), \sin\theta(0)\sin\phi(0), \cos\theta(0)]$. General single-qubit gates can be constructed by selecting different parameters. Universal quantum computation can be realized by a nontrivial two-qubit quantum gate assisted by arbitrary single-qubit gates [112].

For the two-qubit gate, the auxiliary bases can be chosen as

$$|\varphi_1(t)\rangle = |00\rangle,$$

$$|\varphi_2(t)\rangle = \cos\frac{\theta(t)}{2}|01\rangle + \sin\frac{\theta(t)}{2}e^{i\phi(t)}|10\rangle,$$

$$|\varphi_3(t)\rangle = \sin\frac{\theta(t)}{2}e^{-i\phi(t)}|01\rangle - \cos\frac{\theta(t)}{2}|10\rangle,$$

$$|\varphi_4(t)\rangle = |11\rangle. \tag{D5}$$

The general form of the Hamiltonian for realizing a two-qubit gate is

$$\hat{H}_{\text{two}}(t) = i\sum_{k\neq l}^4\langle\varphi_l(t)|\dot{\varphi}_k(t)\rangle|\varphi_l(t)\rangle\langle\varphi_k(t)|, = \frac{\Omega_{\text{two}}(t)}{2}|01\rangle\langle10| + \text{H.c.} \tag{D6}$$

The evolution operator of this system can be expressed as

$$U_2(T) = |\varphi_1(T)\rangle\langle\varphi_1(0)| + e^{-i\gamma(T)}|\varphi_2(0)\rangle\langle\varphi_2(0)| + e^{i\gamma(T)}|\varphi_3(0)\rangle\langle\varphi_3(0)| + \varphi_4(T)\rangle\langle\varphi_4(0)|,$$

$$= \begin{pmatrix} 1 & 0 & 0 & 0 \\ 0 & \cos\gamma(T) - i\cos\theta(0)\sin\gamma(T) & -ie^{-i\varphi(0)}\sin\theta(0)\sin\gamma(T) & 0 \\ 0 & -ie^{i\varphi(0)}\sin\theta(0)\sin\gamma(T) & \cos\gamma(T) + i\cos\theta(0)\sin\gamma(T) & 0 \\ 0 & 0 & 0 & 1 \end{pmatrix}. \tag{D7}$$

By selecting appropriate parameters, we can build a nontrivial two-qubit quantum geometric gate, and the general geometric quantum computation can be achieved by combining it with universal single-qubit gates.

APPENDIX E: QUANTITATIVE THEORY OF FIDELITY AGAINST CONTROL ERROR ϵ

In this section, we provide a quantitative statement on how fluctuations in control parameters affect the system fidelity. We use the effective model and an alternative definition of fidelity to provide an analytical solution for the fluctuation of fidelity with system parameters. For convenience, we utilize a different definition of fidelity $F_\epsilon = (\text{Tr}[U^\dagger U_\epsilon]/\text{Tr}[U^\dagger U])$ [117], where $U_\epsilon(\tau) = \mathcal{T}e^{(-i\int_0^\tau\hat{H}_1'(t)\,dt)}$, $\mathcal{T}$ is the time order operator, and $\hat{H}_1' = (1 + \epsilon)\hat{H}_1$.

For the geometric phase gate, the fidelity is $F_{\epsilon1} = 1/4(2 + \sqrt{2} - (-2 + \sqrt{2})\cos\pi\epsilon)$. Then, expanding the $F_{\epsilon1}$ series to the second order, $F_{\epsilon1} = 1 + 1/8(-2 + \sqrt{2})\pi^2\epsilon^2 + \mathcal{O}(\epsilon^3)$, where $\mathcal{O}(\epsilon^3)$ is the third order, and higher-order expansions can be discarded. Similarly, the quantitative solution for fidelity, $F_{\epsilon2} = \cos(\pi\epsilon/2)^2$, of the dynamical phase gate expanded to the second order is $F_{\epsilon2} = 1 - (\pi^2\epsilon^2/4) + \mathcal{O}(\epsilon^3)$. The fidelity is $F_{\epsilon3} = (\cos((\pi\epsilon/4))^2(2 + (-2 + \sqrt{2})\cos(\pi\epsilon/2)))/\sqrt{2} = 1 + 1/16(-3 + 2\sqrt{2})\pi^2\epsilon^2 + \mathcal{O}(\epsilon^3)$ and $F_{\epsilon4} = \frac{1}{2}(\cos((\pi\epsilon/4)) + \cos((3\pi\epsilon/4))) = 1 - (5\pi^2\epsilon^2/32) + \mathcal{O}(\epsilon^3)$ for the geometric Hadamard gate and the dynamical Hadamard gate, respectively.

Here, we take the Hadamard gate as an example and provide a detailed calculation process to prove that $F_{\epsilon3}$ and $F_{\epsilon4}$ correspond to the NGQC and DQC, respectively. The difference between geometric and dynamic schemes is that, when constructing the same gate, the evolution

path on the Bloch sphere is different. When using NGQC to construct the gate, parameter settings are shown in Eq. (18), and the evolution is divided into three segments. The Hamiltonian is time independent within each segment, and the analytical expression of the evolution operator can be accurately solved. Under the representation of the $\{|0\rangle_L, |1\rangle_L\}$ basis, the Hamiltonian has control error ϵ and the evolution operator of each segment can be represented as

$$
\hat{H}_{h1} = \begin{pmatrix} 0 & (1+\epsilon)\Omega_{\text{eff}}/2 \\ (1+\epsilon)\Omega_{\text{eff}}/2 & 0 \end{pmatrix}, \qquad \hat{U}_{h1} = e^{-i\hat{H}_{h1}t}, \quad t \in [0, T/4],
$$

$$
\hat{H}_{h2} = \begin{pmatrix} 0 & -(1+\epsilon)\Omega_{\text{eff}}/2e^{-i\pi/4} \\ -(1+\epsilon)\Omega_{\text{eff}}/2e^{i\pi/4} & 0 \end{pmatrix}, \quad \hat{U}_{h2} = e^{-i\hat{H}_{h2}t}, \quad t \in (T/4, 3T/4], \tag{E1}
$$

$$
\hat{H}_{h3} = \begin{pmatrix} 0 & (1+\epsilon)\Omega_{\text{eff}}/2 \\ (1+\epsilon)\Omega_{\text{eff}}/2 & 0 \end{pmatrix}, \qquad \hat{U}_{h3} = e^{-i\hat{H}_{h3}t}, \quad t \in (3T/4, T].
$$

The total evolution operator of the Hadamard gate constructed by NGQC with control error ϵ is

$$
\hat{U}_\epsilon = \hat{U}_{h3} \cdot \hat{U}_{h2} \cdot \hat{U}_{h1},
$$

$$
= \begin{pmatrix} \frac{1}{4}\left(\left(\sqrt{2}-2\right)\cos(\pi\epsilon) + \sqrt{2}+2\right) & \frac{\cos\left(\frac{\pi\epsilon}{2}\right)}{\sqrt{2}} - \frac{i}{4}\left(\sqrt{2}-2\right)\sin(\pi\epsilon) \\ -\frac{\cos\left(\frac{\pi\epsilon}{2}\right)}{\sqrt{2}} - \frac{1}{4}i\left(\sqrt{2}-2\right)\sin(\pi\epsilon) & \frac{1}{4}\left(\left(\sqrt{2}-2\right)\cos(\pi\epsilon) + \sqrt{2}+2\right). \end{pmatrix}. \tag{E2}
$$

Then, using $F_\epsilon = (\mathrm{Tr}[U^\dagger U_\epsilon]/\mathrm{Tr}[U^\dagger U])$, it can be concluded that $F_{\epsilon 3} = (\cos((\pi\epsilon/4))^2(2 + (-2 + \sqrt{2})\cos(\pi\epsilon/2)))/\sqrt{2} = 1 + 1/16(-3 + 2\sqrt{2})\pi^2\epsilon^2 + \mathcal{O}(\epsilon^3)$.

For the Hadamard gate constructed by DQC, the Hamiltonian has control error ϵ and the evolution operator of each segment can be represented as

$$
\hat{H}_{hd1} = \begin{pmatrix} 0 & e^{-i\pi/2}(1+\epsilon)\Omega_{\text{eff}}/2 \\ e^{i\pi/2}(1+\epsilon)\Omega_{\text{eff}}/2 & 0 \end{pmatrix}, \quad \hat{U}_{hd1} = e^{-i\hat{H}_{hd1}t}, \quad t \in [0, T/3],
$$

$$
\hat{H}_{hd2} = \begin{pmatrix} 0 & (1+\epsilon)\Omega_{\text{eff}}/2 \\ (1+\epsilon)\Omega_{\text{eff}}/2 & 0 \end{pmatrix}, \qquad \hat{U}_{hd2} = e^{-i\hat{H}_{hd2}t}, \quad t \in (T/3, T]. \tag{E3}
$$

The total evolution operator of the Hadamard gate constructed by DQC with control error ϵ is

$$
\hat{U}_\epsilon = \hat{U}_{hd2} \cdot \hat{U}_{hd1},
$$

$$
= \begin{pmatrix} -\frac{1+i}{2}\left(-i\sin\left(\frac{3\pi - \epsilon\pi}{4}\right) - \cos\left(\frac{\pi - 3\epsilon\pi}{4}\right)\right) & -\frac{1+i}{2}\left(\cos\left(\frac{3\pi\epsilon + \pi}{4}\right) + i\sin\left(\frac{\epsilon\pi + \pi}{4}\right)\right) \\ \frac{1-i}{2}\left(\cos\left(\frac{3\pi\epsilon + \pi}{4}\right) - i\sin\left(\frac{\pi\epsilon + \pi}{4}\right)\right) & \frac{1+i}{2}\left(\cos\left(\frac{\epsilon\pi + \pi}{4}\right) + i\sin\left(\frac{3\pi\epsilon + \pi}{4}\right)\right) \end{pmatrix}. \tag{E4}
$$

The fidelity of the Hadamard gate constructed by DQC can be calculated as $F_{\epsilon 4} = \frac{1}{2}(\cos((\pi\epsilon/4)) + \cos((3\pi\epsilon/4))) = 1 - (5\pi^2\epsilon^2/32) + \mathcal{O}(\epsilon^3)$. Other analytical expressions can be calculated in the same way.

From Fig. 10, it is obvious that, as ϵ increases, the fidelity of each gate decreases, and the numerical results simulated through the master equation are highly consistent with our analytical solution. The deviation comes from different fidelity-solving methods and high-order fluctuation of F_ϵ.

APPENDIX F: IMPLEMENTATION OF DYNAMIC GATES IN NUMERICAL COMPARISON

Different from our geometric implementation of quantum gates, the implementation of dynamical quantum gates in a numerical comparison is explained here. The dynamic
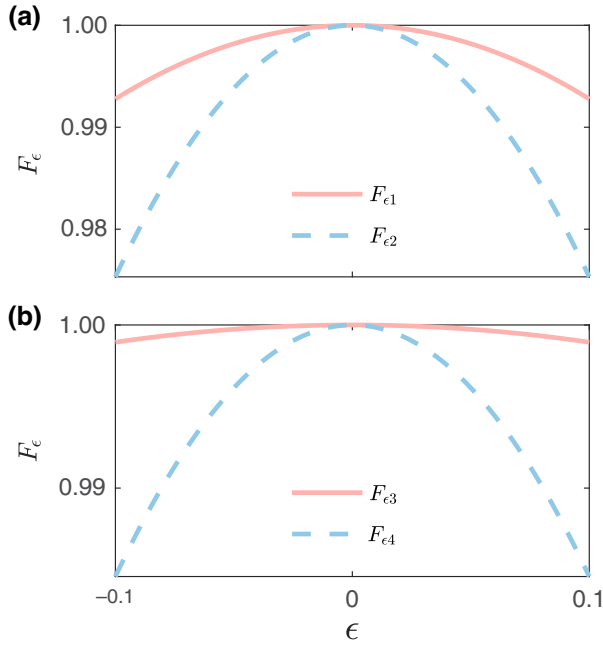
(a)

(b)

FIG. 10. Fidelity, F_ϵ, of the phase gate (a) and the Hadamard gate (b) against control error. Among them, $F_{\epsilon 1}$ and $F_{\epsilon 3}$ represent the phase gate and the Hadamard gate constructed by NGQC, while $F_{\epsilon 2}$ and $F_{\epsilon 4}$ correspond to the phase gate and the Hadamard gate constructed by DQC.

evolution operator of Eq. (11) is

$$
U_d(\theta_d, \varphi) = \begin{pmatrix} \cos\theta_d & -i\sin\theta_d e^{i\varphi} \\ -i\sin\theta_d e^{-i\varphi} & \cos\theta_d \end{pmatrix}, \quad \text{(F1)}
$$

where $\theta_d = \frac{1}{2}\int_0^{\tau_d} |\Omega_{\text{eff}}|\, dt$. Based on this, the Hadamard gate and the phase gate in Sec. III A can be realized by $U_d((\pi/4), -(\pi/2))U_d((\pi/2), 0)$ and $U_d(-(\pi/2), 0)U_d(-(\pi/2), (\pi/2))U_d((\pi/2), 0)$, respectively. In addition, to ensure fairness in the comparison, the amplitude of the Rabi frequency is selected to be the same as that of the geometric gates.

APPENDIX G: QUANTITATIVE THEORY OF FIDELITY AGAINST THE FLUCTUATION OF THE EFFECT OF THE ENVIRONMENT η

Here, we discuss the impact of the environment-system interaction strength on system fidelity. To quantify the impact of the interaction strength of environmental systems on fidelity, we add a fluctuation of η to the strength of the interaction, that is, $\hat{H}_I \to (1 + \eta)\hat{H}_I$. For convenience, we discuss the evolution of the system in the interaction scenario, so we let $\hat{H}_0 = \hat{H}_1 \otimes \mathbb{I}_E + \mathbb{I}_S \otimes \hat{H}_E$ and $U = e^{-i\hat{H}_0 t/\hbar}$. The relationship between the density operator under the interaction scenario, $\tilde{\rho}_{\text{tol}}$, and the density operator under the Schrödinger scenario, ρ_{tol}, is

$$
\tilde{\rho}_{\text{tol}}(t) = U^\dagger(t)\rho_{\text{tol}}(t)U(t). \quad \text{(G1)}
$$

The time evolution of the total density matrix is

$$
\frac{d\tilde{\rho}_{\text{tol}}(t)}{dt} = \frac{1}{i\hbar}[\tilde{\hat{H}}_I(t), \tilde{\rho}_{\text{tol}}(t)], \quad \text{(G2)}
$$

where $\tilde{\hat{H}}_I(t) = U^\dagger(t)\hat{H}_I(t)U(t)$. We expand the solution of $\tilde{\rho}_{\text{tol}}(t)$ to the second order:

$$
\tilde{\rho}_{\text{tol}}(t) = \tilde{\rho}_{\text{tol}}(0) + \frac{1+\eta}{i\hbar}\int_0^t ds[\tilde{\hat{H}}_I(s), \tilde{\rho}_{\text{tol}}(s)] - \frac{(1+\eta)^2}{\hbar^2}\int_0^t ds_1 \int_0^{s_1} ds_2[\tilde{\hat{H}}_I(s_1), [\tilde{\hat{H}}_I(s_2), \tilde{\rho}_{\text{tol}}(s_2)]]. \quad \text{(G3)}
$$

We only focus on the evolution of the system:

$$
\frac{d\tilde{\rho}(t)}{dt} = \text{Tr}_E\left[\frac{d\tilde{\rho}_{\text{tol}}(t)}{dt}\right] = \frac{1+\eta}{i\hbar}\text{Tr}_E[\tilde{\hat{H}}_I(s), \tilde{\rho}_{\text{tol}}(s)] - \frac{(1+\eta)^2}{\hbar^2}\int_0^t ds\,\text{Tr}_E[\tilde{\hat{H}}_I(t), [\tilde{\hat{H}}_I(s), \tilde{\rho}_{\text{tol}}(s)]]. \quad \text{(G4)}
$$

Assuming the initial state is $\tilde{\rho}_{\text{tol}}(0) = \tilde{\rho}(0) \otimes \tilde{\rho}_E(t)$ and $\langle E_i \rangle = \text{Tr}[E_i\rho_E(0)] = 0$, that is, under the Born approximation and Markov approximation [118], and the interaction Hamiltonian in the interaction scenario is $\tilde{\hat{H}}_I = \sum_\alpha \tilde{A}_\alpha(t) \otimes \tilde{B}_\alpha(t)$, the evolution of the system can be written as

$$
\begin{aligned}
\frac{d\tilde{\rho}(t)}{dt} &= -\frac{(1+\eta)^2}{\hbar^2}\int_0^\infty ds\,\text{Tr}_E[\tilde{\hat{H}}_I(t), [\tilde{\hat{H}}_I(t-s), \tilde{\rho}(t) \otimes \tilde{\rho}_E]], \\
&= -\frac{(1+\eta)^2}{\hbar^2}\int_0^\infty ds\,\text{Tr}_E[\tilde{\hat{H}}_I(t-s)\tilde{\rho}(t) \otimes \tilde{\rho}_E\tilde{\hat{H}}_I(t) - \tilde{\hat{H}}_I(t)\tilde{\hat{H}}_I(t-s)\tilde{\rho}(t) \otimes \tilde{\rho}_E] + \text{H.c.}, \\
&= \sum_{\omega,\omega',\alpha,\beta} e^{i(\omega'-\omega)t}\Gamma_{\alpha\beta}(\omega)[\hat{A}_\beta(\omega)\tilde{\rho}(t), \hat{A}_\alpha^\dagger(\omega')] + \Gamma_{\alpha\beta}^*(\omega)[\hat{A}_\alpha(\omega')\tilde{\rho}(t), \hat{A}_\beta^\dagger(\omega)], \quad \text{(G5)}
\end{aligned}
$$

where $\Gamma_{\alpha\beta}(\omega) = ((1+\eta)^2/\hbar^2)\int_0^\infty ds e^{i\omega s}\mathrm{Tr}_E[\tilde{B}_\alpha^\dagger(s)\tilde{B}_\beta(0)$ $\tilde{\rho}_E]$ Then, applying the rotating-wave approximation,

$$\frac{d\tilde{\rho}(t)}{dt} = \sum_{\omega,\alpha,\beta}\Gamma_{\alpha\beta}(\omega)[\hat{A}_\beta(\omega)\tilde{\rho}(t),\hat{A}_\alpha^\dagger(\omega)]$$
$$+ \Gamma_{\alpha\beta}^*(\omega)[\hat{A}_\alpha(\omega)\tilde{\rho}(t),\hat{A}_\beta^\dagger(\omega)]. \quad (G6)$$

Then, decomposing $\Gamma_{\alpha\beta}(\omega)$ into Hermitian and anti-Hermitian parts,

$$\gamma(\omega) = \Gamma_{\alpha\beta}(\omega) + \Gamma_{\alpha\beta}^*(\omega),$$
$$\Delta(\omega) = \frac{1}{2i}[\Gamma_{\alpha\beta}(\omega) - \Gamma_{\alpha\beta}^*(\omega)]. \quad (G7)$$

Going back to the Schrödingerr scenario, there will only be one relevant frequency, ω, so the evolution is

$$\frac{d\rho(t)}{dt} = -i[\hat{H}_1 + \hat{H}_{LS}, \rho(t)]$$
$$+ \sum_k \gamma_k\left[\hat{L}_k\rho(t)\hat{L}_k^\dagger - \frac{1}{2}\{\hat{L}_k^\dagger\hat{L}_k, \rho(t)\}\right], \quad (G8)$$

where $\hat{L}_k = \mathcal{O}_{k\beta} = \hat{A}_\beta$, $\mathcal{O}$ is a unitary operator, $\mathcal{O}\gamma\mathcal{O}^\dagger$ is a diagonal matrix, and $\hat{H}_{LS} = \hbar\sum_{\alpha\beta}\Delta_{\alpha\beta}\hat{A}_\alpha^\dagger\hat{A}_\beta$ is called a

Lamb shift. It will cause a shift in the position of the energy levels, and its impact on the Hamiltonian of the system can generally be ignored [119].

Then, the effective Hamiltonian of a system can be approximated in its simplest form [120] as

$$\hat{H}_{\eta 1} = \begin{pmatrix} 0 & \frac{|\Omega_{\mathrm{eff}}|}{2}e^{i\varphi} \\ \frac{|\Omega_{\mathrm{eff}}|}{2}e^{-i\varphi} & -i(1+\eta)^2\frac{\gamma}{2} \end{pmatrix}, \quad (G9)$$

where the decay rating of our system is assumed to be $(\gamma/2) = |\Omega_{\mathrm{eff}}|/100$ (reasonable and can simplify calculations). Using $F_\eta = (\mathrm{Tr}[U^\dagger U_\eta]/\mathrm{Tr}[U^\dagger U])$ to solve the fidelity of the interaction strength varies with the system environment, where $U_\eta(\tau) = \mathcal{T}e^{(-i\int_0^\tau \hat{H}_1'(t)dt)}$. From Fig. 8, we can see that the fidelity curves of CDD and PDDs are almost parallel to the curve without DD; the impact of the environment on system fidelity is almost the same in the presence or absence of DD. Here, we take the phase gate as an example, so the Hamiltonian of each segment can be written as (the Hamiltonian of each segment is time independent)

$$\hat{H}_{p1} = \begin{pmatrix} 0 & \Omega_{\mathrm{eff}}/2 \\ \Omega_{\mathrm{eff}}/2 & -i(1+\eta)^2\Omega_{\mathrm{eff}}/100 \end{pmatrix}, \qquad \hat{U}_{p1} = e^{-i\hat{H}_{p1}T/2}, \quad t \in [0, T/2],$$
$$\hat{H}_{p2} = \begin{pmatrix} 0 & e^{i\pi/4}\Omega_{\mathrm{eff}}/2 \\ e^{-i\pi/4}\Omega_{\mathrm{eff}}/2 & -i(1+\eta)^2\Omega_{\mathrm{eff}}/100 \end{pmatrix}, \quad \hat{U}_{p2} = e^{-i\hat{H}_{p2}T/2}, \quad t \in (T/2, T]. \quad (G10)$$

The total evolution operator of the phase gate constructed by DQC with the fluctuation of the environment, ϵ, is

$$\hat{U}_\eta = \hat{U}_{hd2} \cdot \hat{U}_{hd1}. \quad (G11)$$

Then, we have

$$F_{\eta 1} = \frac{1}{2x}\left(\left[-\eta_- e^{-\frac{\pi\eta_-}{200}} + \eta_+ e^{-\frac{\pi\eta_+}{200}}\right]\left[\frac{i}{2x}\sqrt{x}\exp\left(-\frac{\pi\eta_+}{200}\right)\right]\right.$$
$$+ \frac{1}{8(ix)^{3/2}}\left[\sqrt{x}\left\{\left[-\eta_-\exp\left(-\frac{\pi\eta_+}{200}\right) + \eta_+\exp\left(\frac{\eta_-\pi}{200}\right)\right]\sqrt{2}\left[(1+i)\left\{2\sqrt{x}\exp\left(-\frac{\pi\eta_+}{200}\right)\right\}\right]\right.$$
$$\left.\left.-2500\left(\frac{i}{(ix)^{3/2}}+1\right)\left(-1+e^{\frac{-\pi\sqrt{x}}{100}}\right)\left(e^{\frac{\pi\sqrt{x}}{100}}-1\right)\exp\left(-\frac{\pi\eta_1^2}{100}\right)\right\}\right]\right), \quad (G12)$$

where $\eta_1 = \eta + 1$, $x = \eta_1^4 - 10000$, $\eta_+ = \eta_1^2 + \sqrt{x}$, and $\eta_- = \eta_1^2 - \sqrt{x}$. By expanding Eq. (G12) to the second order of η_1 and using numerical fitting, we can obtain $F_\eta = 1 - 0.01\eta_1 - 0.0225\eta_1^2 + \mathcal{O}(\eta_1^3)$. The fidelity can be improved by minimizing the impact of η_1 on the system as

much as possible. The DD used in the manuscript is one of the methods.

The fidelity, F_η, of the phase gate varies with η, as shown in Fig. 11, and the consistency with the values in Fig. 8 is very high. It is obvious that, as η increases, the
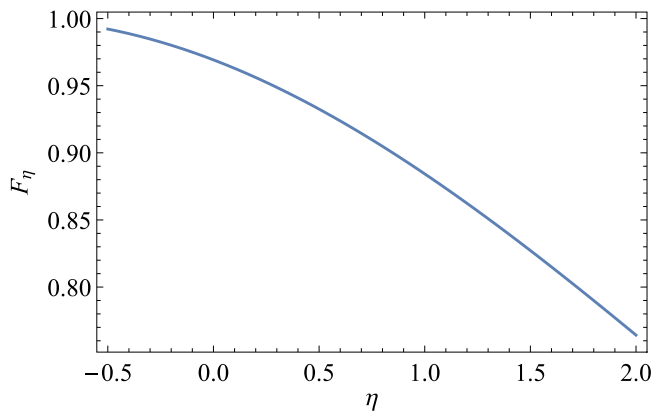
FIG. 11. Fidelity, F_η, variation with the fluctuation of the effect of environment, η, of the phase gate.

fidelity will decrease. The slight deviation comes from different solving methods of fidelity.

[1] S. Pezzagna and J. Meijer, Quantum computer based on color centers in diamond, Appl. Phys. Rev. **8,** 011308 (2021).

[2] M.-R. Yun, F.-Q. Guo, L.-L. Yan, E. Liang, Y. Zhang, S.-L. Su, C. X. Shan, and Y. Jia, Parallel-path implementation of nonadiabatic geometric quantum gates in a decoherence-free subspace with nitrogen-vacancy centers, Phys. Rev. A **105,** 012611 (2022).

[3] Z. Jin, S. L. Su, and S. Zhang, Preparation of a steady entangled state of two nitrogen-vacancy centers by simultaneously utilizing two dissipative factors, Phys. Rev. A **100,** 052332 (2019).

[4] J. Zhou, W.-C. Yu, Y.-M. Gao, and Z.-Y. Xue, Cavity QED implementation of non-adiabatic holonomies for universal quantum gates in decoherence-free subspaces with nitrogen-vacancy centers, Opt. Express **23,** 14027 (2015).

[5] P.-B. Li, S.-Y. Gao, H.-R. Li, S.-L. Ma, and F.-L. Li, Dissipative preparation of entangled states between two spatially separated nitrogen-vacancy centers, Phys. Rev. A **85,** 042306 (2012).

[6] F. Jelezko, T. Gaebel, I. Popa, A. Gruber, and J. Wrachtrup, Observation of coherent oscillations in a single electron spin, Phys. Rev. Lett. **92,** 076401 (2004).

[7] B. Li, P.-B. Li, Y. Zhou, S.-L. Ma, and F.-L. Li, Quantum microwave-optical interface with nitrogen-vacancy centers in diamond, Phys. Rev. A **96,** 032342 (2017).

[8] L. Rondin, J.-P. Tetienne, T. Hingant, J.-F. Roch, P. Maletinsky, and V. Jacques, Magnetometry with nitrogen-vacancy defects in diamond, Rep. Prog. Phys. **77,** 056503 (2014).

[9] M. W. Doherty, N. B. Manson, P. Delaney, F. Jelezko, J. Wrachtrup, and L. C. Hollenberg, The nitrogen-vacancy colour centre in diamond, Phys. Rep. **528,** 1 (2013). the nitrogen-vacancy colour centre in diamond.

[10] L. Childress, R. Walsworth, and M. Lukin, Atom-like crystal defects: From quantum computers to biological sensors, Phys. Today **67,** 38 (2014).

[11] Y. Wang, H.-L. Zhang, J.-L. Wu, J. Song, K. Yang, W. Qin, H. Jing, and L.-M. Kuang, Quantum parametric amplification of phonon-mediated magnon-spin interaction, Sci. China Phys., Mech. Astron. **66,** 110311 (2023).

[12] H. Bernien, B. Hensen, W. Pfaff, G. Koolstra, M. S. Blok, L. Robledo, T. H. Taminiau, M. Markham, D. J. Twitchen, L. Childress, and R. Hanson, Heralded entanglement between solid-state qubits separated by three metres, Nature **497,** 86 (2013).

[13] A. Sipahigil, R. E. Evans, D. D. Sukachev, M. J. Burek, J. Borregaard, M. K. Bhaskar, C. T. Nguyen, J. L. Pacheco, H. A. Atikian, C. Meuwly, R. M. Camacho, F. Jelezko, E. Bielejec, H. Park, M. Lončar, and M. D. Lukin, An integrated diamond nanophotonics platform for quantum-optical networks, Science **354,** 847 (2016).

[14] A. Dietrich, K. D. Jahnke, J. M. Binder, T. Teraji, J. Isoya, L. J. Rogers, and F. Jelezko, Isotopically varying spectral features of silicon-vacancy in diamond, New J. Phys. **16,** 113019 (2014).

[15] J. N. Becker and C. Becher, Coherence properties and quantum control of silicon vacancy color centers in diamond, Phys. Status Solidi (A) **214,** 1700586 (2017).

[16] E. Londero, G. M. H. Thiering, L. Razinkovas, A. Gali, and A. Alkauskas, Vibrational modes of negatively charged silicon-vacancy centers in diamond from *ab initio* calculations, Phys. Rev. B **98,** 035306 (2018).

[17] S. Meesala, Y.-I. Sohn, B. Pingault, L. Shao, H. A. Atikian, J. Holzgrafe, M. Gündoğan, C. Stavrakas, A. Sipahigil, C. Chia, R. Evans, M. J. Burek, M. Zhang, L. Wu, J. L. Pacheco, J. Abraham, E. Bielejec, M. D. Lukin, M. Atatüre, and M. Lončar, Strain engineering of the silicon-vacancy center in diamond, Phys. Rev. B **97,** 205444 (2018).

[18] P. Udvarhelyi, R. Nagy, F. Kaiser, S.-Y. Lee, J. Wrachtrup, and A. Gali, Spectrally stable defect qubits with no inversion symmetry for robust spin-to-photon interface, Phys. Rev. Appl. **11,** 044022 (2019).

[19] M. W. Day, K. M. Bates, C. L. Smallwood, R. C. Owen, T. Schröder, E. Bielejec, R. Ulbricht, and S. T. Cundiff, Coherent interactions between silicon-vacancy centers in diamond, Phys. Rev. Lett. **128,** 203603 (2022).

[20] C. Hepp, T. Müller, V. Waselowski, J. N. Becker, B. Pingault, H. Sternschulte, D. Steinmüller-Nethl, A. Gali, J. R. Maze, M. Atatüre, and C. Becher, Electronic structure of the silicon vacancy color center in diamond, Phys. Rev. Lett. **112,** 036405 (2014).

[21] L. J. Rogers, K. D. Jahnke, M. H. Metsch, A. Sipahigil, J. M. Binder, T. Teraji, H. Sumiya, J. Isoya, M. D. Lukin, P. Hemmer, and F. Jelezko, All-optical initialization, readout, and coherent preparation of single silicon-vacancy spins in diamond, Phys. Rev. Lett. **113,** 263602 (2014).

[22] B. Pingault, D.-D. Jarausch, C. Hepp, L. Klintberg, J. N. Becker, M. Markham, C. Becher, and M. Atatüre, Coherent control of the silicon-vacancy spin in diamond, Nat. Commun. **8,** 15579 (2017).

[23] M.-A. Lemonde, S. Meesala, A. Sipahigil, M. J. A. Schuetz, M. D. Lukin, M. Loncar, and P. Rabl, Phonon networks with silicon-vacancy centers in diamond waveguides, Phys. Rev. Lett. **120,** 213603 (2018).

[24] Y.-F. Qiao, J.-Q. Chen, X.-L. Dong, B.-L. Wang, X.-L. Hei, C.-P. Shen, Y. Zhou, and P.-B. Li, Generation

of Greenberger-Horne-Zeilinger states for silicon-vacancy centers using a decoherence-free subspace, Phys. Rev. A **105**, 032415 (2022).

[25] X. Li, S. Ma, J. Xie, Y. Ren, and F. Li, Dissipative generation of steady-state entanglement of two separated SiV$^-$ centers coupled to photonic crystal cavities, Quantum Inf. Process. **19**, 301 (2020).

[26] G. Thiering and A. Gali, *Ab initio* magneto-optical spectrum of group-IV vacancy color centers in diamond, Phys. Rev. X **8**, 021063 (2018).

[27] S. Häußler, G. Thiering, A. Dietrich, N. Waasem, T. Teraji, J. Isoya, T. Iwasaki, M. Hatano, F. Jelezko, A. Gali, and A. Kubanek, Photoluminescence excitation spectroscopy of SiV$^-$ and GeV$^-$ color center in diamond, New J. Phys. **19**, 063036 (2017).

[28] T. D. Ladd, F. Jelezko, R. Laflamme, Y. Nakamura, C. Monroe, and J. L. O'Brien, Quantum computers, Nature **464**, 45 (2010).

[29] Y.-F. Qiao, H.-Z. Li, X.-L. Dong, J.-Q. Chen, Y. Zhou, and P.-B. Li, Phononic-waveguide-assisted steady-state entanglement of silicon-vacancy centers, Phys. Rev. A **101**, 042313 (2020).

[30] J.-Q. Chen, Y.-F. Qiao, X.-L. Dong, X.-L. Hei, and P.-B. Li, Dissipation-assisted preparation of steady spin-squeezed states of SiV centers, Phys. Rev. A **103**, 013709 (2021).

[31] B. Li, X. Li, P. Li, and T. Li, Preparing squeezed spin states in a spin-mechanical hybrid system with silicon-vacancy centers, Adv. Quantum Technol. **3**, 2000034 (2020).

[32] X.-X. Li, B. Li, and P.-B. Li, Simulation of topological phases with color center arrays in phononic crystals, Phys. Rev. Res. **2**, 013121 (2020).

[33] P. Solinas, P. Zanardi, and N. Zanghì, Robustness of non-Abelian holonomic quantum gates against parametric noise, Phys. Rev. A **70**, 042316 (2004).

[34] S.-L. Zhu and P. Zanardi, Geometric quantum gates that are robust against stochastic control errors, Phys. Rev. A **72**, 020301 (2005).

[35] M. V. Berry, Quantal phase factors accompanying adiabatic changes, Proc. R. Soc. London. A. Math. Phys. Sci. **392**, 45 (1984).

[36] F. Wilczek and A. Zee, Appearance of gauge structure in simple dynamical systems, Phys. Rev. Lett. **52**, 2111 (1984).

[37] J. Anandan, Non-adiabatic non-Abelian geometric phase, Phys. Lett. A **133**, 171 (1988).

[38] Y. Aharonov and J. Anandan, Phase change during a cyclic quantum evolution, Phys. Rev. Lett. **58**, 1593 (1987).

[39] J. A. Jones, V. Vedral, A. Ekert, and G. Castagnoli, Geometric quantum computation using nuclear magnetic resonance, Nature **403**, 869 (2000).

[40] P. Zanardi and M. Rasetti, Holonomic quantum computation, Phys. Lett. A **264**, 94 (1999).

[41] W. Xiang-Bin and M. Keiji, Nonadiabatic conditional geometric phase shift with NMR, Phys. Rev. Lett. **87**, 097901 (2001).

[42] S.-L. Zhu and Z. D. Wang, Implementation of universal quantum gates based on nonadiabatic geometric phases, Phys. Rev. Lett. **89**, 097902 (2002).

[43] E. Sjöqvist, D. M. Tong, L. M. Andersson, B. Hessmo, M. Johansson, and K. Singh, Non-adiabatic holonomic quantum computation, New J. Phys. **14**, 103035 (2012).

[44] C.-Y. Guo, L.-L. Yan, S. Zhang, S.-L. Su, and W. Li, Optimized geometric quantum computation with a mesoscopic ensemble of Rydberg atoms, Phys. Rev. A **102**, 042607 (2020).

[45] M. Yun, F.-Q. Guo, M. Li, L.-L. Yan, M. Feng, Y.-X. Li, and S.-L. Su, Distributed geometric quantum computation based on the optimized-control-technique in a cavity-atom system via exchanging virtual photons, Opt. Express **29**, 8737 (2021).

[46] M. Li, F.-Q. Guo, Z. Jin, L.-L. Yan, E.-J. Liang, and S.-L. Su, Multiple-qubit controlled unitary quantum gate for Rydberg atoms using shortcut to adiabaticity and optimized geometric quantum operations, Phys. Rev. A **103**, 062607 (2021).

[47] T. Chen and Z.-Y. Xue, Nonadiabatic geometric quantum computation with parametrically tunable coupling, Phys. Rev. Appl. **10**, 054051 (2018).

[48] T. Chen and Z.-Y. Xue, High-fidelity and robust geometric quantum gates that outperform dynamical ones, Phys. Rev. Appl. **14**, 064009 (2020).

[49] C.-Y. Ding, Y. Liang, K.-Z. Yu, and Z.-Y. Xue, Nonadiabatic geometric quantum computation with shortened path on superconducting circuits, Appl. Phys. Lett. **119**, 184001 (2021).

[50] S. Li, J. Xue, T. Chen, and Z.-Y. Xue, High-fidelity geometric quantum gates with short paths on superconducting circuits, Adv. Quantum Technol. **4**, 2000140 (2021).

[51] B.-J. Liu, S.-L. Su, and M.-H. Yung, Nonadiabatic noncyclic geometric quantum computation in Rydberg atoms, Phys. Rev. Res. **2**, 043130 (2020).

[52] N. Eivarsson and E. Sjöqvist, Genuinely noncyclic geometric gates in two-pulse schemes, Phys. Rev. A **108**, 032612 (2023).

[53] Y.-H. Kang, Y.-H. Chen, X. Wang, J. Song, Y. Xia, A. Miranowicz, S.-B. Zheng, and F. Nori, Nonadiabatic geometric quantum computation with cat-state qubits via invariant-based reverse engineering, Phys. Rev. Res. **4**, 013233 (2022).

[54] K. Z. Li, P. Z. Zhao, and D. M. Tong, Approach to realizing nonadiabatic geometric gates with prescribed evolution paths, Phys. Rev. Res. **2**, 023295 (2020).

[55] W. Li, Invariant-based inverse engineering for fast nonadiabatic geometric quantum computation, New J. Phys. **23**, 073039 (2021).

[56] J. Zhou, S. Li, G.-Z. Pan, G. Zhang, T. Chen, and Z.-Y. Xue, Nonadiabatic geometric quantum gates that are insensitive to qubit-frequency drifts, Phys. Rev. A **103**, 032609 (2021).

[57] B.-J. Liu, X.-K. Song, Z.-Y. Xue, X. Wang, and M.-H. Yung, Plug-and-play approach to nonadiabatic geometric quantum gates, Phys. Rev. Lett. **123**, 100501 (2019).

[58] K. Z. Li, G. F. Xu, and D. M. Tong, Coherence-protected nonadiabatic geometric quantum computation, Phys. Rev. Res. **3**, 023104 (2021).

[59] B.-J. Liu, Y.-S. Wang, and M.-H. Yung, Super-robust nonadiabatic geometric quantum control, Phys. Rev. Res. **3**, L032066 (2021).

[60] Y. Du, Z. Liang, H. Yan, and S. Zhu, Geometric quantum computation with shortcuts to adiabaticity, Adv. Quantum Technol. **2,** 1900013 (2019).

[61] F.-Q. Guo, X.-Y. Zhu, L.-L. Yan, M. Feng, and S.-L. Su, Distinguishment of Greenberger–Horne–Zeilinger states in Rydberg atoms via noncyclic geometric quantum computation, Ann. Phys. **533,** 2100057 (2021).

[62] J.-J. Cheng and L. Zhang, Implementing conventional and unconventional nonadiabatic geometric quantum gates via SU(2) transformations, Phys. Rev. A **103,** 032616 (2021).

[63] Y. Xu, Z. Hua, T. Chen, X. Pan, X. Li, J. Han, W. Cai, Y. Ma, H. Wang, Y. P. Song, Z.-Y. Xue, and L. Sun, Experimental implementation of universal nonadiabatic geometric quantum gates in a superconducting circuit, Phys. Rev. Lett. **124,** 230503 (2020).

[64] T. Yan, B.-J. Liu, K. Xu, C. Song, S. Liu, Z. Zhang, H. Deng, Z. Yan, H. Rong, K. Huang, M.-H. Yung, Y. Chen, and D. Yu, Experimental realization of nonadiabatic shortcut to non-Abelian geometric gates, Phys. Rev. Lett. **122,** 080501 (2019).

[65] J. W. Zhang, L.-L. Yan, J. C. Li, G. Y. Ding, J. T. Bu, L. Chen, S.-L. Su, F. Zhou, and M. Feng, Single-atom verification of the noise-resilient and fast characteristics of universal nonadiabatic noncyclic geometric quantum gates, Phys. Rev. Lett. **127,** 030502 (2021).

[66] M.-Z. Ai, S. Li, Z. Hou, R. He, Z.-H. Qian, Z.-Y. Xue, J.-M. Cui, Y.-F. Huang, C.-F. Li, and G.-C. Guo, Experimental realization of nonadiabatic holonomic single-qubit quantum gates with optimal control in a trapped ion, Phys. Rev. Appl. **14,** 054062 (2020).

[67] Y. Dong, S.-C. Zhang, Y. Zheng, H.-B. Lin, L.-K. Shan, X.-D. Chen, W. Zhu, G.-Z. Wang, G.-C. Guo, and F.-W. Sun, Experimental implementation of universal holonomic quantum computation on solid-state spins with optimal control, Phys. Rev. Appl. **16,** 024060 (2021).

[68] Y.-Y. Huang, Y.-K. Wu, F. Wang, P.-Y. Hou, W.-B. Wang, W.-G. Zhang, W.-Q. Lian, Y.-Q. Liu, H.-Y. Wang, H.-Y. Zhang, L. He, X.-Y. Chang, Y. Xu, and L.-M. Duan, Experimental realization of robust geometric quantum gates with solid-state spins, Phys. Rev. Lett. **122,** 010503 (2019).

[69] D. A. Lidar, I. L. Chuang, and K. B. Whaley, Decoherence-free subspaces for quantum computation, Phys. Rev. Lett. **81,** 2594 (1998).

[70] L.-A. Wu, P. Zanardi, and D. A. Lidar, Holonomic quantum computation in decoherence-free subspaces, Phys. Rev. Lett. **95,** 130501 (2005).

[71] A. Beige, D. Braun, B. Tregenna, and P. L. Knight, Quantum computing using dissipation to remain in a decoherence-free subspace, Phys. Rev. Lett. **85,** 1762 (2000).

[72] P. G. Kwiat, A. J. Berglund, J. B. Altepeter, and A. G. White, Experimental verification of decoherence-free subspaces, Science **290,** 498 (2000).

[73] D. A. Lidar and K. Birgitta Whaley, in *Irreversible Quantum Dynamics*, edited by F. Benatti and R. Floreanini (Springer Berlin Heidelberg, Berlin, Heidelberg, 2003), p. 83.

[74] D. Bacon, J. Kempe, D. A. Lidar, and K. B. Whaley, Universal fault-tolerant quantum computation on

[75] decoherence-free subspaces, Phys. Rev. Lett. **85,** 1758 (2000).

[75] G. F. Xu, J. Zhang, D. M. Tong, E. Sjöqvist, and L. C. Kwek, Nonadiabatic holonomic quantum computation in decoherence-free subspaces, Phys. Rev. Lett. **109,** 170501 (2012).

[76] P. Xue and Y.-F. Xiao, Universal quantum computation in decoherence-free subspace with neutral atoms, Phys. Rev. Lett. **97,** 140501 (2006).

[77] M.-D. Choi and D. W. Kribs, Method to find quantum noiseless subsystems, Phys. Rev. Lett. **96,** 050501 (2006).

[78] L. Viola, E. M. Fortunato, M. A. Pravia, E. Knill, R. Laflamme, and D. G. Cory, Experimental realization of noiseless subsystems for quantum information processing, Science **293,** 2059 (2001).

[79] J. Zhang, L.-C. Kwek, E. Sjöqvist, D. M. Tong, and P. Zanardi, Quantum computation in noiseless subsystems with fast non-Abelian holonomies, Phys. Rev. A **89,** 042302 (2014).

[80] E. M. Fortunato, L. Viola, M. A. Pravia, E. Knill, R. Laflamme, T. F. Havel, and D. G. Cory, Exploring noiseless subsystems via nuclear magnetic resonance, Phys. Rev. A **67,** 062303 (2003).

[81] D. A. Lidar, in *Quantum Information and Computation for Chemistry* (John Wiley & Sons, Ltd, New York, 2014), p. 295.

[82] L. Viola, E. Knill, and S. Lloyd, Dynamical decoupling of open quantum systems, Phys. Rev. Lett. **82,** 2417 (1999).

[83] A. M. Souza, G. A. Álvarez, and D. Suter, Robust dynamical decoupling, Philos. Trans. R. Soc. A: Math., Phys. Eng. Sci. **370,** 4748 (2012).

[84] K. Khodjasteh and D. A. Lidar, Fault-tolerant quantum dynamical decoupling, Phys. Rev. Lett. **95,** 180501 (2005).

[85] M. J. Biercuk, H. Uys, A. P. VanDevender, N. Shiga, W. M. Itano, and J. J. Bollinger, Optimized dynamical decoupling in a model quantum memory, Nature **458,** 996 (2009).

[86] G. Xu and G. Long, Protecting geometric gates by dynamical decoupling, Phys. Rev. A **90,** 022323 (2014).

[87] P. Z. Zhao, X. Wu, and D. M. Tong, Dynamical-decoupling-protected nonadiabatic holonomic quantum computation, Phys. Rev. A **103,** 012205 (2021).

[88] X. Wu and P. Z. Zhao, Nonadiabatic geometric quantum computation protected by dynamical decoupling via the *XXZ* Hamiltonian, Front. Phys. **17,** 31502 (2021).

[89] X. Wu and P. Z. Zhao, Universal nonadiabatic geometric gates protected by dynamical decoupling, Phys. Rev. A **102,** 032627 (2020).

[90] X.-L. Zhen, F.-H. Zhang, G. Feng, H. Li, and G.-L. Long, Optimal experimental dynamical decoupling of both longitudinal and transverse relaxations, Phys. Rev. A **93,** 022304 (2016).

[91] F. F. Fanchini, R. D. J. Napolitano, B. Çakmak, and A. O. Caldeira, Protecting the $\sqrt{\text{SWAP}}$ operation from general and residual errors by continuous dynamical decoupling, Phys. Rev. A **91,** 042325 (2015).

[92] A. M. Souza, G. A. Álvarez, and D. Suter, Experimental protection of quantum gates against decoherence and control errors, Phys. Rev. A **86,** 050301 (2012).

[93] W. Morong, K. Collins, A. De, E. Stavropoulos, T. You, and C. Monroe, Engineering dynamically decoupled quantum simulations with trapped ions, PRX Quantum **4,** 010334 (2023).

[94] L. Viola, S. Lloyd, and E. Knill, Universal control of decoupled quantum systems, Phys. Rev. Lett. **83,** 4888 (1999).

[95] E. L. Hahn, Spin echoes, Phys. Rev. **80,** 580 (1950).

[96] K. Khodjasteh and D. A. Lidar, Rigorous bounds on the performance of a hybrid dynamical-decoupling quantum-computing scheme, Phys. Rev. A **78,** 012355 (2008).

[97] A. M. Steane, Overhead and noise threshold of fault-tolerant quantum error correction, Phys. Rev. A **68,** 042322 (2003).

[98] K. Khodjasteh and L. Viola, Dynamically error-corrected gates for universal quantum computation, Phys. Rev. Lett. **102,** 080501 (2009).

[99] K. Khodjasteh, D. A. Lidar, and L. Viola, Arbitrarily accurate dynamical control in open quantum systems, Phys. Rev. Lett. **104,** 090501 (2010).

[100] H. A. Jahn, E. Teller, and F. G. Donnan, Stability of polyatomic molecules in degenerate electronic states - I—orbital degeneracy, Proc. R. Soc. London. Ser. A - Math. Phys. Sci. **161,** 220 (1937).

[101] B. Pingault, J. N. Becker, C. H. H. Schulte, C. Arend, C. Hepp, T. Godde, A. I. Tartakovskii, M. Markham, C. Becher, and M. Atatüre, All-optical formation of coherent dark states of silicon-vacancy spins in diamond, Phys. Rev. Lett. **113,** 263601 (2014).

[102] J. N. Becker, B. Pingault, D. Groß, M. Gündoğan, N. Kukharchyk, M. Markham, A. Edmonds, M. Atatüre, P. Bushev, and C. Becher, All-optical control of the silicon-vacancy spin in diamond at millikelvin temperatures, Phys. Rev. Lett. **120,** 053603 (2018).

[103] F. S. Ham, Dynamical Jahn-Teller effect in paramagnetic resonance spectra: Orbital reduction factors and partial quenching of spin-orbit interaction, Phys. Rev. **138,** A1727 (1965).

[104] K. V. Kepesidis, M.-A. Lemonde, A. Norambuena, J. R. Maze, and P. Rabl, Cooling phonons with phonons: Acoustic reservoir engineering with silicon-vacancy centers in diamond, Phys. Rev. B **94,** 214115 (2016).

[105] D. F. James and J. Jerke, Effective Hamiltonian theory and its applications in quantum information, Can. J. Phys. **85,** 625 (2007).

[106] E. Brion, L. H. Pedersen, and K. Mølmer, Adiabatic elimination in a lambda system, J. Phys. A: Math. Theor. **40,** 1033 (2007).

[107] P. Tamarat, T. Gaebel, J. R. Rabeau, M. Khan, A. D. Greentree, H. Wilson, L. C. L. Hollenberg, S. Prawer, P. Hemmer, F. Jelezko, and J. Wrachtrup, Stark shift control of single optical centers in diamond, Phys. Rev. Lett. **97,** 083002 (2006).

[108] V. M. Acosta, C. Santori, A. Faraon, Z. Huang, K.-M. C. Fu, A. Stacey, D. A. Simpson, K. Ganesan, S. Tomljenovic-Hanic, A. D. Greentree, S. Prawer, and R. G. Beausoleil, Dynamic stabilization of the optical resonances of single nitrogen-vacancy centers in diamond, Phys. Rev. Lett. **108,** 206401 (2012).

[109] B. W. Shore and P. L. Knight, The Jaynes-Cummings model, J. Mod. Opt. **40,** 1195 (1993).

[110] L. Childress, M. V. G. Dutt, J. M. Taylor, A. S. Zibrov, F. Jelezko, J. Wrachtrup, P. R. Hemmer, and M. D. Lukin, Coherent dynamics of coupled electron and nuclear spin qubits in diamond, Science **314,** 281 (2006).

[111] N. Zhao, S.-W. Ho, and R.-B. Liu, Decoherence and dynamical decoupling control of nitrogen vacancy center electron spins in nuclear spin baths, Phys. Rev. B **85,** 115303 (2012).

[112] M. J. Bremner, C. M. Dawson, J. L. Dodd, A. Gilchrist, A. W. Harrow, D. Mortimer, M. A. Nielsen, and T. J. Osborne, Practical scheme for quantum computation with any two-qubit entangling gate, Phys. Rev. Lett. **89,** 247902 (2002).

[113] J. R. West, D. A. Lidar, B. H. Fong, and M. F. Gyure, High fidelity quantum gates via dynamical decoupling, Phys. Rev. Lett. **105,** 230503 (2010).

[114] N. Schuch and J. Siewert, Natural two-qubit gate for quantum computation using the XY interaction, Phys. Rev. A **67,** 032301 (2003).

[115] J. Wang, Y. Zhou, X. Zhang, F. Liu, Y. Li, K. Li, Z. Liu, G. Wang, and W. Gao, Efficient generation of an array of single silicon-vacancy defects in silicon carbide, Phys. Rev. Appl. **7,** 064021 (2017).

[116] M. C. M. O'Brien and C. C. Chancey, The Jahn–Teller effect: An introduction and current review, Am. J. Phys. **61,** 688 (1993). https://pubs.aip.org/aapt/ajp/article-pdf/61/8/688/12168801/688_1_online.pdf.

[117] S. Li, B.-J. Liu, Z. Ni, L. Zhang, Z.-Y. Xue, J. Li, F. Yan, Y. Chen, S. Liu, M.-H. Yung, Y. Xu, and D. Yu, Superrobust geometric control of a superconducting circuit, Phys. Rev. Appl. **16,** 064003 (2021).

[118] D. Manzano and P. Hurtado, Harnessing symmetry to control quantum transport, Adv. Phys. **67,** 1 (2018).

[119] D. Manzano, A short introduction to the Lindblad master equation, AIP Adv. **10,** 025106 (2020).

[120] A. J. Daley, Quantum trajectories and open many-body quantum systems, Adv. Phys. **63,** 77 (2014).